BBA - Proteins and Proteomics 1873 (2025) 141072

Contents lists available at ScienceDirect

BBA - Proteins and Proteomics

journal homepage: www.elsevier.com/locate/bbapap

Role of electrostatics in cold adaptation: A comparative study of eury- and stenopsychrophilic triose phosphate isomerase

Jan S. Nowak [a], Sune Olesen [a], Pengfei Tian [b], René L. Bærentsen [c], Ditlev E. Brodersen [c], Daniel E. Otzen [a,c,*]

[a] Interdisciplinary Nanoscience Center (iNANO), Aarhus University, Gustav Wieds Vej 14, 8000 Aarhus C, Denmark
[b] Flagship Labs 97, Inc, 55 Cambridge Parkway, Cambridge 02142, MA, USA
[c] Department of Molecular Biology and Genetics, Aarhus University, Universitetsbyen 81, 8000 Aarhus C, Denmark

ARTICLE INFO

Keywords:
Cold-active enzyme
Thermal stability
Unfolding kinetics
Chemical denaturants
Machine learning model

ABSTRACT

Psychrophilic (cold-active) organisms have developed enzymes that facilitate sufficient metabolic activity at low temperatures to sustain life. This occurs through molecular adaptations that tend to increase protein flexibility at the expense of stability. However, psychrophiles also vary in their growth conditions. Eurypsychrophiles thrive over a wide temperature range and often prefer temperatures above 20 °C, while stenopsychrophiles grow optimally below 15 °C and are more narrowly adapted to cold temperatures. To elucidate differences between these two classes of enzymes, we here compare the stability and unfolding kinetics of two orthologues of the basal household enzyme triose phosphate isomerase, one from the stenopsychrophilic Antarctic permafrost bacterium *Rhodonellum psychrophilum* (sTPI) and the other from the eurypsychrophilic Greenland ikaite column bacterium *Rhodococcus* sp. *JG-3* (eTPI). Remarkably, sTPI proved significantly more thermostable and resistant to chemical denaturation than its eurypsychrophilic counterpart, eTPI, in the absence of ionic components in solution, whereas inclusion of electrostatic screening agents in the form of sodium chloride or the charged denaturant guanidinium chloride largely cancelled out this difference. Thus, electrostatics play a prominent role in stabilizing the stenopsychrophilic sTPI, and a mandatory low-temperature growth environment does not preclude the development of considerable thermotolerance for individual enzymes. We were able to increase the thermostability of sTPI using an evolutionary machine learning model, which transferred several sTPI residues into the eTPI active site. While the stabilizing effect was modest, the combination of individual mutations was additive, underscoring the potential of combining multiple beneficial mutations to achieve enhanced enzyme properties.

1. Introduction

Psychrophilic bacteria thrive in cold (≤5 °C) environments such as polar and tundra biomes and deep oceans [1]. Adaptation to low growth temperatures is reflected at the molecular level. The organisms have overcome many cold-related challenges, including lower membrane fluidity, increased viscosity, higher redox potential, protein cold denaturation, and a general reduction in chemical (and hence enzymatic) reactivity [1]. Furthermore, growth at subzero temperatures usually requires high salt concentrations to avoid freezing, which poses an osmotic challenge for the bacteria. Although genomic and proteomic studies show psychrophilic bacteria to be a highly diverse group of organisms, they are broadly divided into two categories based on their specific temperature profiles [2]. Eurypsychrophiles can grow at subzero temperatures but typically have their optimal growth temperature above 20 °C and characteristically thrive over a wide temperature range [3]. For example, *Rhodococcus* sp. *JG-3*, isolated from Antarctic permafrost soil, grows from 30 °C down to at least −5 °C, with optimal growth at ~20 °C [4]. In contrast, stenopsychrophiles are more narrowly adapted to low temperatures and typically grow optimally

Abbreviations: CD, circular dichroism; DSF, differential scanning fluorimetry; eTPI, triose phosphate isomerase from the eurypsychrophile *Rhodococcus* sp. *JG-3*; GAP, glyceraldehyde 3-phosphate; GDH, glycerol-3-phosphate dehydrogenase; NADH, nicotinamide adenine dinucleotide; sTPI, triose phosphate isomerase from the stenopsychrophile *Rhodonellum psychrophilum*; TPI, triose phosphate isomerase.

* Corresponding author at: Interdisciplinary Nanoscience Center (iNANO), Aarhus University, Gustav Wieds Vej 14, 8000 Aarhus C, Denmark.
E-mail address: dao@inano.au.dk (D.E. Otzen).

https://doi.org/10.1016/j.bbapap.2025.141072
Received 30 December 2024; Received in revised form 27 March 2025; Accepted 31 March 2025
Available online 11 April 2025

below 15 °C. A classic stenopsychrophile is *Rhodonellum psychrophilum* from Greenlandic ikaite tufa columns [5]. This bacterium has a growth range between 22 °C and 0 °C and an optimal growth temperature narrowly centered around 5–10 °C.

These narrow/wide adaptation types suggest significant differences in cold-adaptative strategies and their molecular basis. A general issue for organisms inhabiting cold environments is to maintain sufficient metabolic activity for growth despite low temperatures. This challenge is overcome by enzymes compensating for the usually exponential fall in reaction rates as the temperature declines through comparatively higher flexibility, leading to less temperature-dependent catalysis [6,7]. The high flexibility consequently results in a thermal and chemical [8–10] stability-activity trade-off. Indeed, melting points of psychrophilic enzymes tend to be lower than their meso- and thermophilic orthologues, just as they are significantly more susceptible to chemical denaturants such as urea or guanidinium chloride [8,11,12]. Despite common catalytic features, molecular adaptations of psychrophilic enzymes differ significantly between specific proteins, even within the same protein family [13]. Psychrophilic enzymes tend to have more Gly residues, fewer Pro residues in loops, fewer disulfide bonds, fewer salt bridges, a less packed hydrophobic core, and more hydrophobic patches exposed to solvent [8,13,14]. In addition, the length and mobility of surface loops and alternations in quaternary structure also influence cold adaptation [15–17]. All these adaptations contribute to a more flexible and less stable structure than their meso- and thermophilic counterparts. Some psychrophilic enzymes show a clear gap between (early) inactivation and (late) unfolding events, irrespective of the nature of denaturation [8]. The discrepancy between activity loss and structural unfolding has traditionally been attributed to a highly heat-labile active site [18,19]. However, a more recent hypothesis correlates the optimal temperature of activity t_{opt} with the specific heat capacity of catalytic activation ($\Delta C_p^{\ddagger}$), rather than local unfolding [20,21].

An early biophysical comparison between psychro- meso-, and thermophilic enzymes studied triose phosphate isomerases (TPIs) from three different *Clostridia* species with growth optima at 18 °C, 37 °C, and 55 °C [22]. The bacteria's thermal adaptation was reflected not only in the heat sensitivity of the enzymes but also by their resistance towards chemical denaturation. The rationale for using TPIs to study thermal adaptations is simple: they are small (though dimeric), canonical $(\alpha/\beta)_8$-barrel enzymes which efficiently isomerize glyceraldehyde-3-phosphate (GAP) and dihydroxyacetone phosphate (DHAP) in a crucial metabolic reaction. Moreover, TPIs have been dubbed perfect enzymes due to their very high k_{cat}/K_m-values. The high efficiency and structural conservation make TPIs excellent models to identify subtle differences in thermal adaptation. Indeed, TPIs have helped elucidate structure-function relationships in psychrophilic enzymes, revealing that even small changes in the structure can affect their ability and catalytic efficiency at low temperatures [15,23]. An excellent example is a comparative study of two TPIs from the psychrophilic bacterium *Vibrio marinus* and mesophilic *Escherichia coli,* which identified a single crucial amino acid position responsible for the shift towards heat lability [23].

Most structural studies of psychrophilic enzymes attempt to pinpoint adaptations to catalysis at low temperatures compared to their meso- and thermophilic homologs. This approach has proven to work well in identifying adaptations towards cold in general; however, it does not reflect the potentially high diversity of adaptations within the world of psychrophiles. Here, we investigate whether the difference in evolutionary adaptations of eury- and stenopsychrophilic bacteria are reflected in the structure and functions of their metabolic enzymes. Our reasoning is that central metabolic enzymes are key to an organism's survival and may even constitute "hubs" [24] with biophysical properties that determine the organism's tolerance towards temperature, ionic strength and other external parameters. Therefore, we identified, expressed, and purified two triose phosphate isomerases from the eurypsychrophilic *Rhodococcus* sp. *JG-3* and a stenopsychrophilic *Rhodonellum psychrophilum* to investigate differences in their catalysis and stability and elucidate how this is reflected in their structure. We determined crystal structures of both enzymes and studied their stability through thermal and chemical denaturation. Surprisingly, TPI from *R. psychrophilum* (sTPI) proved far more stable towards heat and chemical denaturant than the TPI from *Rhodococcus* sp. *JG-3* (eTPI). We observed that the stability difference is rooted in electrostatics, as charged denaturants and titration of sodium chloride affected sTPI significantly more than eTPI. We hypothesized that although both enzymes assume the classical $(\beta\alpha)_8$-fold and have perfectly conserved active sites, crucial differences near the catalytic site and the subunit interface may be responsible for differences in stability. To elucidate whether single mutations could stabilize the less stable protein, eTPI, we used an evolutionary machine learning model to identify stabilizing mutations. Strikingly, three of the top four high-scoring mutations involved amino acids that also occur in the same positions in the more stable protein, sTPI. We prepared and studied these four mutations individually and combined in a quadruple mutant. We discovered that they stabilized eTPI without compromising enzymatic activity, although the increase in t_m of ~3 °C was modest compared to the ~23 °C difference between eTPI and the more stable sTPI. This indicates that the active site only contributes to a small extent to the difference in stability.

2. Methods

Plasmid design: Whole-length gene sequences of TPIs from *Rhodococcus sp JG-3* (NCBI:WP_027497007.1, here eTPI) and *Rhodonellum psychrophilum* (NCBI:WP_019596507.1, here sTPI) were codon-optimized for expression in *E. coli* with GeneSmart (GenScript, New Jersey, USA). pET 28a(+) plasmids with the optimized sequences were provided by GenScript using *Nde*I/Xhol restriction sites, resulting in an N-terminal His_6 tag in front of the thrombin cleavage site (sequences provided in **Supplementary Table S1**).

Protein expression: Plasmids were transformed into *E. coli* BL21 (DE3) with an Electroporator 2510 (Eppendorf, Hamburg, Germany) using single pulse electroporation at 1800 V, after which the cells were incubated in a Gene Pulser® electroporation cuvette (Bio-rad, Hercules, CA) with 0.5 mL of Super Optimal with Catabolite repression (SOC) medium for 1 h at 37 °C, spread on an LB agar plate containing 50 μg/mL kanamycin (kan) and grown O/N at 37 °C. A single colony was picked and suspended in 1–2 mL LB-kan medium, spread onto eight LB-kan agar plates and grown O/N at 37 °C. The cells were transferred into 1 L LB-kan medium in 2 L flasks, grown in shaking incubators (37 °C, 180 rpm) until OD_{600} ~ 0.8, induced with 1 mM Isopropyl β-D-1-thio-galactopyranoside and then incubated 4 h at 20 °C. The cells were harvested by spinning at 4000 x *g* at 4 °C for 30 mins in a Sorvall Lynx 6000 centrifuge (Thermo Fisher, Waltham, MA). The supernatant was discarded, and the pellet was dissolved in 10 mL of buffer A (50 mM Hepes-OH, 100 mM NaCl, pH 7.5) including 10 mM imidazole and stored at −20 °C.

Protein purification: Thawed cells were lysed using a Q500 sonicator (Qsonica, Newtown, CT) with a 2 mm microtip probe set to 20 s pulses with a 10 s pause at 20 % intensity over 10 min. The lysate was centrifuged at 15.000 x*g* in a Sorvall Lynx 6000 centrifuge for 20 min at 4 °C. The supernatant was filtered through a 0.45 μm syringe filter and incubated with Ni(II) charged Ni-NTA beads (Thermo Fisher) at 4 °C for 10 min, followed by a wash with buffer A including 40 mM imidazole and elution with buffer A including 400 mM imidazole. The eluted solution was immediately exchanged to buffer A using a PD-10 desalting column and further purified by size exclusion chromatography using a Superdex 200 Increase 10/300 GL column (Cytiva, Marlborough, MA) connected to an Äkta Pure 25 M system (Cytiva, Marlborough, USA).

Thermal denaturation by CD: Circular dichroism experiments were performed using a Chirascan-plus CD spectropolarimeter (Applied Photophysics, Leatherhead, UK) equipped with a TC1 Temperature controller (Quantum Northwest, Liberty Lake, WA). Far-UV experiments were performed with 0.1 mg/mL protein in buffer A in a 1 mm quartz

cuvette (Hellma, Buchs, Switzerland), while near-UV experiments were performed at 1 mg/mL in a 5 mm quartz cuvette. The sample was measured with 1 nm bandwidth at 200–260 nm for far-UV CD and 250–320 nm for near-UV CD. Both experiments were performed with 0.5 °C/min gradient in steps of 1 °C step from 10 °C to 90 °C. The resulting unfolding curves were analyzed using Global 3 Thermal Global Analysis Software (Applied Photophysics, Leatherhead, UK), which utilizes the following Eq. [25]:

$$\theta_t = (a_F T + b_F - a_U T + b_U)\left(1 + e^{\left(\frac{\Delta H}{R}\right)\left(\frac{1}{T}-\frac{1}{T_m}\right)}\right) + m_U T + b_U \quad (1)$$

Here θ_t is the measured ellipticity, a_F and a_U are the temperature-dependent slopes and b_F and b_F are the baseline values for the folded and the unfolded state, respectively. ΔH is the unfolding enthalpy, T_m is the melting temperature, and T is temperature (both in Kelvin). The software fits multiple transitions over the measured wavelengths, treating ΔH and T_m as global variables while a_F, a_U, b_F and b_F are local variables.

Isothermal unfolding kinetics at elevated temperatures measured by CD: Isothermal unfolding kinetics experiments were performed by setting the CD instrument at a temperature near their optimal activity temperature (40–51 °C for eTPI and 60–75 °C for sTPI) and monitoring ellipticity at 222 nm. 0.1 mg/mL protein in buffer A was inserted in a 1 mM quartz cuvette with a digital thermometer probe that continuously measured the temperature of the protein solution as it asymptotically approaches a stable value during the experiment ($t_{½}$ for thermal equilibration was 30–50 s). Each experiment provided a time profile for CD and temperature, with data recorded every 0.5 s. Data were analyzed numerically in Excel using Solver, where exponential decay was approximated as a linear equation in small time intervals much smaller than the $t_{½}$ of the reaction. In practice, the difference in signal between time t and $t + \Delta t$ caused by a reaction rate constant k was calculated as $-k^* \Delta t$, in which k was assumed to be temperature dependent in an Arrhenius fashion, i.e. $k_{unf}^{T} = k_{unf}^{T\,end}$*exp.((−$E_a$/R)*(1/$T$-1/$T_{end}$)). The variables used were the activation energy E_a and the rate constant at the end-level temperature $k_{unf}^{T\,end}$ reached in the cuvette during the experiment, typically within a few minutes. This approach essentially fitted the whole reaction time profile and provided a robust estimate of the unfolding rate $k_{unf}^{T\,end}$ at the end-level temperature T_{end}. The activation energy E_a was not used for further analysis.

Thermal denaturation by DSF: DSF experiments were performed on a Prometheus Panta apparatus (NanoTemper Technologies, München, Germany). 0.1 mg/mL protein in buffer A was transferred by capillary action into a NT.48 capillary and heated up with a 1 °C/min gradient between 15 °C and 90 °C. Fluorescence emission was recorded at 330 nm and 350 nm (excitation at 280 nm), and the ratio between emission at 330 and 350 nm was fitted to eq. 2 (an expanded version of eq. 1 using base 10 exponentials and curvature in the denatured state) [26] using GraphPad Prism 9 (San Diego, California, USA):

$$\theta = \frac{(\alpha_N + \beta_N T) + (\alpha_D + \beta_D T + \gamma_D T^2)\ 10^{-\frac{\Delta H_{Tm}\left(1-\frac{T}{T_m}\right)}{RT}}}{1 + 10^{-\frac{\Delta H_{Tm}\left(1-\frac{T}{T_m}\right)}{RT}}} \quad (2)$$

Parameters are defined as in eq. 1; in addition, γ_D is a constant which takes into account curvature in the denatured state baseline. Free energy of unfolding at a given temperature, $\Delta G(T)$, is given as [26]:

$$\Delta G(T) = \Delta H_{Tm}\left(1 - \frac{T_m}{T}\right) - \Delta C_p\left(T - T_m + \ln\left(\frac{T_m}{T}\right)\right) \quad (3)$$

Here, ΔC_p is the change in heat capacity upon unfolding, which is the slope of a plot between ΔH_{Tm} and T_m obtained from thermal scans recorded at different denaturant concentrations and fitted using eq. 3. Note that both TPI molecules are dimers and formally this should be included in the analysis of the denaturation curves. However, thermal scans of eTPI at 2 and 0.02 mg/mL between 0 and 4 M urea did not reveal any systematic increase in stability at the higher concentration; furthermore, there was no clear increase in T_m between 0.015 and 1 mg/mL protein for either protein when measured in 0.5 M GdmCl (data not shown). In addition, thermal denaturation is completely irreversible for both proteins (data not shown). For ease of comparison, we restrict ourselves to a reversible and monomeric unfolding system, although neither assumption is formally upheld. This does not detract from the main focus of this study, which is to compare the stabilities of the two TPI proteins under otherwise identical conditions.

Chemical denaturation: Unfolding of eTPI and sTPI was monitored over time at 25 °C using 0.1 mg/mL TPI in buffer A and different concentrations of denaturant (urea or GdmCl) in steps of 0.25 M. Unfolding >2 M guanidinium chloride (leading to unfolding half times $t_{½} \leq 3$ min, dead time of manual mixing ~10–15 s) was monitored on a LS55 fluorimeter (Perkin-Elmer, MA), with excitation at 280 nm and emission at 350 nm (eTPI) or 325 nm (sTPI) measured every 1 s. Unfolding at lower guanidinium chloride concentrations was measured in a Clariostar plate reader (BMG Biosciences) using excitation at 280 nm and emission at 330 and 350 nm (dead time of manual mixing ~2 min). 150 µl samples were shaken at 200 rpm for 30 s before each measurement (carried out every 100 s). Time curves were fitted to a single exponential decay:

$$F = Amp^* e^{-kt} + c \quad (4)$$

where F is the measured fluorescence, Amp is the amplitude and k the rate constant of the associated fluorescence signal and c is the offset. The offset represents the signal at equilibrium and was plotted versus denaturant concentration ([den]) according to the Eq. [27]:

$$c = \frac{(\alpha_N + \beta_N[den]) + (\alpha_D + \beta_D[den])^* 10^{m_{D-N}^*\left([den] - [den]^{50\%}\right)/-RT}}{1 + 10^{m_{D-N}^*\left([den] - [den]^{50\%}\right)/-RT}} \quad (5)$$

Here α_N and α_D are the baseline values of the native and denatured state, β_N and β_D are the denaturant-dependent slopes of these two baselines, $[den]^{50\%}$ is the midpoint of denaturation and $m_{D\text{-}N}$ is the dependence of the base 10 logarithm of the equilibrium constant $K_{D—N}$ on denaturant concentration.

For refolding experiments, sTPI and eTPI were first unfolded at 1 mg/mL protein in either 5 M urea or 2 M GdmCl by incubation overnight at room temperature. Refolding was initiated by dilution into buffer and different concentrations of denaturant, monitored kinetically as for unfolding and fitted to inverted exponential decays to obtain the end-point plateau fluorescence.

Continuous coupled enzyme assay: The activity of TPI was determined as described [28]. Briefly, reactions were performed in Nunc 96-well UV Plates (Fisher, Massachusetts, USA) using 0.6 mM glyceraldehyde 3-phosphate (GAP, TPI substrate), 0.3 mM nicotinamide adenine dinucleotide (NADH, GDH cofactor) and 10 µg/mL glycerol-3-phosphate dehydrogenase (GDH, downstream enzyme). The reaction was initiated by the addition of 0.1 µg/mL TPI. Before the experiments, GDH was exchanged to buffer A using multiple spins through a disposable 10 kDa spin filter (Merck, New Jersey, USA). TPI transforms GAP into DHAP, which GDH reduces to G3P using NADH.

$$GAP \Leftrightarrow^{TPI} DHAP$$

$$DHAP + NADH \Leftrightarrow^{GDH} G3P + NAD^+$$

Oxidation of NADH leads to a change in absorption at 340 nm, measured on a Clariostar Plus Microplate Reader (BMG Labtech, Ortenberg, Germany). The reaction rate (k_{cat}), expressed in µmol

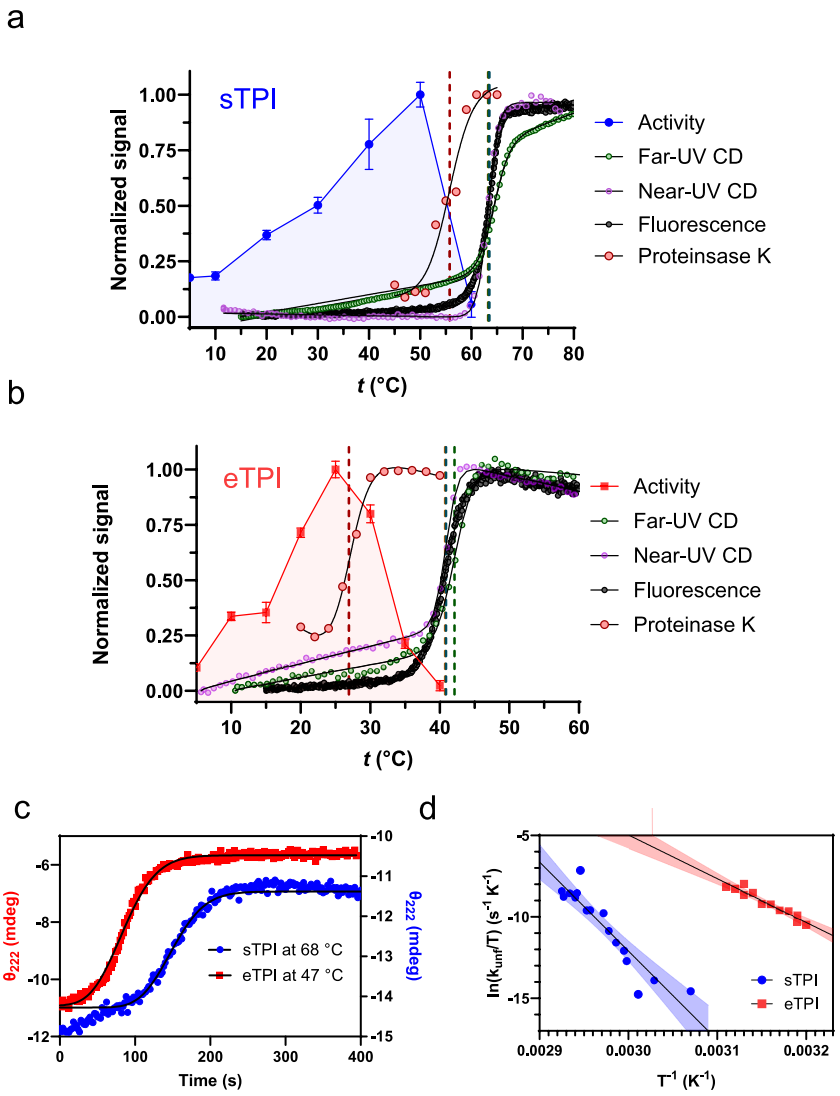

Fig. 1. General biophysical measurements of eTPI and sTPI. **a** + **b**: Normalized equilibrium temperature effects on (**a**) sTPI and (**b**) eTPI represented by initial velocity in enzymatic assays (sTPI, blue circles; eTPI, red squares), Proteinase K (PK) susceptibility (red circles), far-UV CD at 222 nm (green circles), near-UV CD at 260 nm (purple circles), and DSF measured by fluorescence shift 350 nm/330 nm (black circles). The colour-coded, drop-down dotted lines represent midpoint transition values. **c**: Examples of thermal unfolding kinetics measured by CD at 222 nm of sTPI (blue circles) and eTPI (red squares), here shown at 68 °C and 47 °C, respectively. Black lines show best numerical fit to an unfolding model where the rate constant follows Arrhenius temperature dependence. **d**: Eyring plot for unfolding rates recorded at different temperatures for sTPI (blue circles) and eTPI (red squares). A 95 % confidence interval for linear regression is shown by a semitransparent area fill. (For interpretation of the references to colour in this figure legend, the reader is referred to the web version of this article.)

product per min per mg enzyme (U/mg), was calculated using an extinction coefficient of oxidized NADH of 6200 M^{-1} cm^{-1}.

Quenched coupled enzyme assay: To separate TPI activity measurements from the stability of the coupling enzyme GDH under conditions which compromise enzyme stability, we first let TPI react with GAP, after which samples were removed, quenched at low pH to irreversibly denature TPI and then returned to neutral pH and incubated with GDH. The quenched assay was performed by mixing a 700 µL reaction mix of TPI and GAP in 15 mM HEPES-OH, pH 7.5 at a final concentration of 14 ng/mL TPI and 3 mM GAP. Every 2 min, 80 µl of reaction mix was quenched by transfer to 20 µl of 150 mM HCl (leading to ca. 24 mM HCl, i.e. pH ~1.6, after titration of remaining HEPES buffer) and incubation for 1 min. Next, the reaction was mixed with 85 ng/mL GDH, 0.3 mM NADH, and 10 mM EDTA in 50 mM HEPES-OH, pH 7.5. The reaction was followed for 1 min at 340 nm in 1 cm quartz cuvettes on a Lambda 25 UV/VIS spectrophotometer with a PTP-1 Peltier System (PerkinElmer, Massachusetts, USA) set to 25 °C.

Proteinase K assay: TPI was incubated at 0.1 mg/mL with 50 µg/mL proteinase K in 10 mM sodium phosphate pH 7.5 at different temperatures (10–30 °C for eTPI and 45–65 °C for sTPI, in both cases in steps of 2 °C) for 1 h. The reaction was then stopped by adding isopropanol to 2.5 mM, after which the sample was run on SDS-PAGE and the amount of intact TPI was estimated by densitometric scanning using ImageJ [29]. Band intensities were normalized so that untreated (proteinase K-free) samples correspond to 0 % and completely degraded samples to 100 %.

Crystallization, data collection and refinement, and analysis: eTPI and sTPI were purified by gel filtration in a 150 mM Tris-HCl, 100 mM NaCl, pH 7.5 buffer, followed by concentration to 10 mg/mL using a disposable Amicon Ultra 0.5 mL 10 kDa centrifugal spin filter (Merck Millipore). The enzymes used for 300 nL (150 nL protein +150 nL crystallization solution) sitting drops in MRC 2-well crystallization plates using a Mosquito crystal Nanolitre crystallization robot (SPT Labtech, Cambridge, UK) preloaded with 70 µl PEG/Ion (Hampton, CA, USA) crystallization kit, and incubated at 19 °C for two days. sTPI formed crystals in 0.2 M lithium acetate and 20 % *w/v* polyethylene glycol 3350, while eTPI formed crystals in 0.2 sodium fluoride and 20 %

w/v polyethylene glycol 3350. Crystals were harvested in loops and stored in liquid nitrogen in their respective crystallization buffers with the addition of 25 % glycerol for cryoprotection. Single-crystal diffraction data were collected at beamline P14, EMBL-Hamburg, Germany. Diffraction data were processed using XDS [30]. Lattice parameters and space groups were refined through iterative runs of XYCORR, INIT, COLSPOT, IDXREF, and DEFPIX. Unit cell dimensions were confirmed, and data quality metrics, including mosaicity and resolution cutoffs, were assessed through CORRECT and XDSSTAT. Data scaling and resolution limits were determined using XSCALE. Space groups were verified using POINTLESS within CCP4i [31], and Matthews coefficients were calculated to estimate the number of molecules per asymmetric unit. Initial phases were obtained via molecular replacement using PHENIX.phaser with homologous models prepared in PHENIX.sculptor. The structures were manually constructed in Coot [32] and refined iteratively using PHENIX.refine [33]. Structure analysis to obtain the predicted solvation and interface free energy of both proteins was performed using PDBePISA [34]. The atomic coordinates and structure factors have been deposited in the Protein Data Bank under the following accession codes: eTPI, PDB ID 9QUU; sTPI, PDB ID 9QUS.

Prediction of mutations that have high evolutionary fitness: Recent studies have demonstrated promising results in applying machine learning models to design protein sequences with novel properties [35,36] Effectively leveraging evolutionary information can further enhance the accuracy of protein fitness prediction [37–39]. Learning from the patterns of sequence variation across diverse organisms can advance protein engineering methods [40]. Therefore, using multiple sequence alignments of protein sequences, we utilized an unsupervised deep learning model, termed "EVE" (Evolutionary model of Variant Effect), for protein engineering that predicts the effects of protein variants based solely on evolutionary data [37]. EVE captures the evolutionary constraints on protein sequences that maintain fitness, thereby predicting the effects of mutations on protein function and stability without relying on labeled data. To engineer eTPI for better stability and activity, we utilized EVE to predict the effects of all possible single-point mutations in eTPI. The model calculated evolutionary fitness for each possible mutation by evaluating the relative likelihood differences between amino acids at each position based on the evolutionary sequence distribution.

3. Results

3.1. eTPI and sTPI unfold locally prior to global unfolding

We expressed both eTPI and sTPI recombinantly in *E. coli* with an N-terminal His-tag (see Methods for details). Both proteins expressed to very high levels (~15 mg yield per L bacterial culture). The active state of TPI is a dimer with a molecular weight of 59 kDa. To confirm the dimeric state of our two TPI enzymes, we carried out size-exclusion chromatography which showed that both proteins eluted with apparent molecular weights around 90 kDa (**Supplementary Fig. S1**). The apparent molecular weight is higher than expected, and the elongated dimer structure (3.29 nm for eTPI and 3.43 nm for sTPI) cannot fully explain this discrepancy. However, the discrepancy may result from interactions with the size-exclusion column. Consistent with this, BSA, which has a higher molecular weight (66.5 kDa) and a hydrodynamic radius of 3.45 nm, elutes earlier than expected from its molecular weight. In any case, both TPI proteins showed catalytic activity and crystallize in a dimeric arrangement (see below), confirming their native dimeric structure.

We start our biophysical analysis by investigating the thermal stability of eTPI and sTPI, both in terms of activity and structure. For activity measurements, we used a coupled assay, in which TPI converts the substrate D-glyceraldehyde 3-phosphate (GAP) to dihydroxyacetone phosphate (DHAP), after which the enzyme glycerol 3-phosphate dehydrogenase (GDH) converts DHAP to glycerol 3-phosphate (G3P) with NADH as reducing cofactor. In this process, oxidation of NADH to NAD^+ leads to a change in absorption. However, we quickly realized that the down-stream coupling enzyme GDH is heat sensitive with a melting temperature t_m of 41 °C (data not shown), so changes in activity at elevated temperatures could be caused by inactivation of GDH rather than of TPI. To avoid such artefacts, we developed a quenched assay, where TPI was quenched after different periods of time at low (~1.6) pH in HCl, after which the GDH reaction was carried out at 25 °C in a neutralized buffer. This assay provided initial velocities for both TPI enzymes measured from linear increases in product concentration over a 12–24 min period (**Supplementary Fig. S2**) and revealed eTPI to have an optimal activity temperature t_{opt} of 25 °C (Fig. 1a), while sTPI's t_{opt} was measured to be 50 °C (Fig. 1b), i.e. around 25 °C higher. This immediately indicated that sTPI was significantly more thermostable, and by inference more thermodynamically stable, than eTPI. This is amply confirmed in the following sections.

Table 1
Summary of thermal stability parameters for sTPI and eTPI obtained from thermal scans and the temperature dependence of activity and proteinase K sensitivity.

Conditions	Parameter	*eTPI*	*sTPI*
Equilibrium (heat)	t_{opt} [a]	25 °C	50 °C
	t_m (Far-UV CD)[a]	42.1 °C	64.4 °C
	t_m (Near-UV CD) [a]	40.9 °C	63.5 °C
	t_m (DSF) [a]	40.8 °C	63.3 °C
	$t_{50\%}$ (PK) [a]	26.9 °C	55.8 °C
Kinetics (heat)	k_{unf} (t_m) [b]	6.3×10^{-3} s^{-1}	10.6×10^{-3} s^{-1}
	$\Delta H^{\ddagger}_{unfolding}$ [c]	53.4 ± 4.6 kcal/mol	108.6 ± 11.8 kcal/mol
	$\Delta S^{\ddagger}_{unfolding}$ [c]	103.0 ± 10 cal/mol	254.6 ± 30 cal/mol
	$\Delta G^{\ddagger}_{unfolding\ (298K)}$ [c]	22.7 ± 3.0 kcal/mol	32.7 ± 5.2 kcal/mol

Notes:
[a] Melting temperature calculated using eq. 1. Data is found in Fig. 1a and b.
[b] Rate of unfolding calculated using linear regression in Fig. 1d, using melting temperature calculated as the average t_m measured by CD and DSF.
[c] Thermodynamic parameters of activation of unfolding calculated by linear regression of data found in Fig. 1d.

Firstly, we measured the thermal stability of both enzymes using spectroscopic methods, namely far- and near-UV CD (ellipticity in the wavelength region 190–260 nm and 250–320 nm, respectively) and DSF (Trp fluorescence using excitation at 280 nm and the ratio of emissions at 330 and 350 nm). For each enzyme, all three measurement methods agreed on a single sigmoidal transition and provided similar t_m-values for each enzyme. sTPI had a t_m of ~64 °C (Fig. 1a) and eTPI a t_m of ~41 °C (Fig. 1b). Thus, both enzymes lose activity before structural unfolding is detected, whether structure is defined at the secondary (far-UV CD) or tertiary-quaternary (near-UV CD and DSF) level. To probe the emergence of dynamic (and thus protease-sensitive) regions in the global fold of each enzyme, we treated the two enzymes with the conformationally specific heat-stable Proteinase K (ProtK) which preferentially degrades the flexible parts of proteins [24]. We measured the extent of proteolytic cleavage using SDS-PAGE, normalized to the untreated enzyme. Here, we saw that sTPI has a midpoint degradation temperature t_{ProtK} of 55.8 °C (Fig. 1a), while eTPI has a t_{ProtK} of 26.9 °C (Fig. 1b and **Supplementary Fig. S3**). Thus, ProtK treatment of both enzymes showed a transition that matches the loss of activity. For eTPI, the t_{ProtK} is well below the global denaturation temperature t_m, suggesting that inactivation is caused by local loss of structure around the active site rather than global unfolding. In contrast, t_{ProtK} of sTPI is more closely aligned with that of t_m, which is consistent with global unfolding (see Discussion). In agreement with its lower stability in general, eTPI was more sensitive than sTPI towards PK treatment, even below t_{ProtK}, since ~27 % of eTPI, but only 11 % of sTPI, was digested ~5 °C below

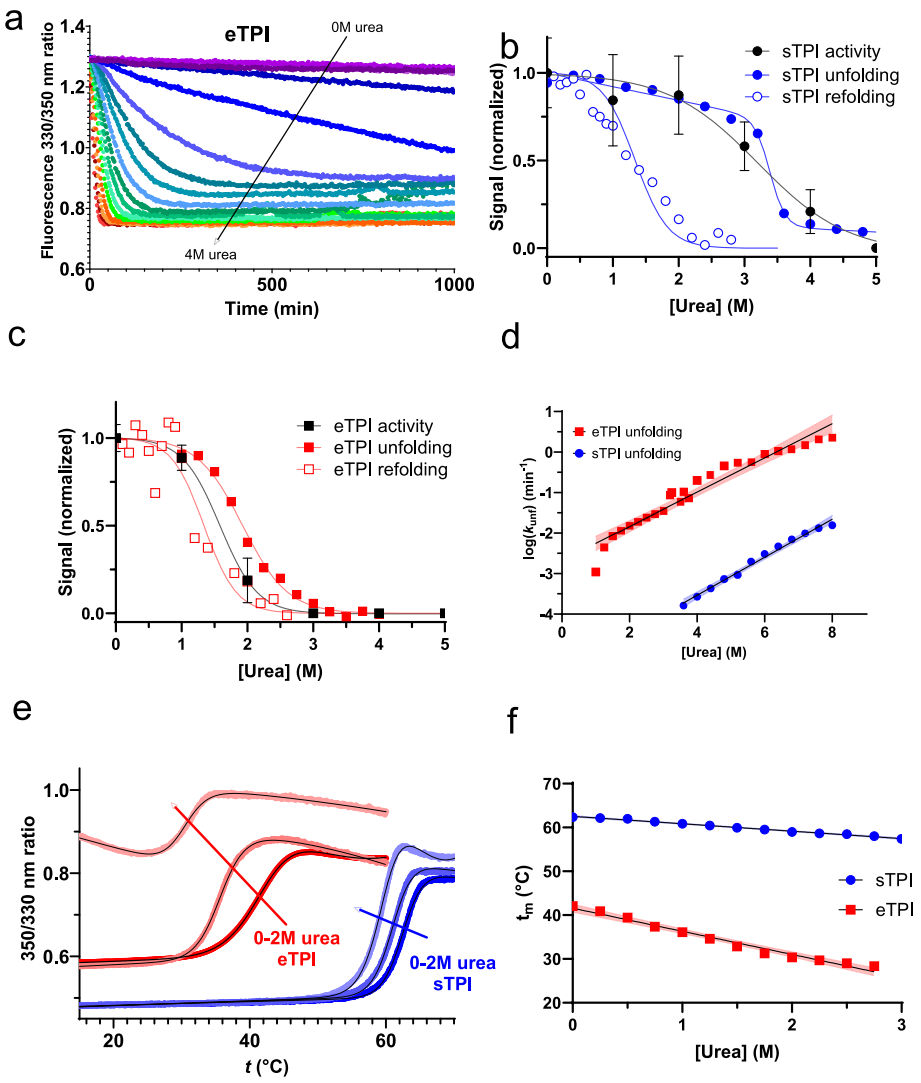

Fig. 2. Effect of urea on TPI stability. **a**: Unfolding kinetics for sTPI (blue) and eTPI (red) in 8 and 1.25 M urea, respectively, fitted with an exponential decay function. **b**: Initial velocity of sTPI in urea (black circles) compared to unfolding (blue circles) and refolding (hollow blue circles) equilibrium data measured by a shift in fluorescence emission from end-point levels of kinetic unfolding and refolding curves. Data are fitted with eq. 2. **c**: Activity of eTPI in urea measured as initial velocity (black squares) compared to unfolding (red squares) and refolding (empty red squares) data measured by a shift in fluorescence emission. Data are fitted with eq. 2. **d**: Log of unfolding rate constants for eTPI (red) and sTPI (blue) as a function of urea concentration. Data are fitted with linear regression, of which a semitransparent area fill shows the 95 % confidence interval. **e**: Examples of DSF thermal unfolding in 0-2 M urea fit with eq. 3. **f**: Change in t_m of sTPI (blue) and eTPI (red) upon titration of urea measured by DSF and fitted with a linear regression where the 95 % confidence intervals are shown as a semitransparent area fill. (For interpretation of the references to colour in this figure legend, the reader is referred to the web version of this article.)

t_{ProtK} (**Fig. 1ab** and **Supplementary Fig. S3**).

Next, we investigated how quickly the two enzymes unfolded at different temperatures by monitoring the far-UV CD signal at temperatures above t_m. We transferred the enzyme from ambient temperatures into a cuvette pre-equilibrated at an elevated temperature while monitoring the temperature in the cuvette using an internal probe in parallel with the CD measurements (Fig. 1c). Unfolding data were fit by numerical analysis that took into account the temperature change during the measurement (see Materials and Methods), providing a rate of unfolding (k_u) at a given temperature (Fig. 1d). An Eyring plot of ln k_u versus 1/T showed a linear correlation in which the intersection with the secondary axis is $\ln\left(\frac{\kappa_B}{h}\right) + \frac{\Delta S^{\ddagger}}{R}$ and the slope of linear regression is $\frac{\Delta H^{\ddagger}}{R}$, where $\Delta S^{\ddagger}$ and $\Delta H^{\ddagger}$ are the activation entropy and enthalpy of unfolding, respectively, as summarized in Table 1. $\Delta H^{\ddagger}$ for sTPI is 108.6 ± 11.8 kcal/mol, which is almost exactly twice that of eTPI with 53.4 ± 4.6 kcal/mol. Similarly, the $\Delta S^{\ddagger}$ of sTPI is 254.6 ± 30 cal/mol, more than twice the value of 103.0 ± 10 cal/mol for eTPI. The two sets of values do not cancel out, resulting in a $\Delta G^{\ddagger}$ (Gibb's free energy of activation $\Delta G^{\ddagger} = \Delta H^{\ddagger} - T\Delta S^{\ddagger}$) of 33.0 kcal/mol for sTPI and 22.7 ± 3.0 kcal/mol for eTPI at 25 °C. Thus, the thermally more stable of the two enzymes (sTPI) also has a higher activation barrier to unfolding, indicating a connection between thermal and kinetic stability.

3.2. eTPI is less stable in urea than sTPI

Having observed a significant difference in thermal stability and unfolding kinetics between eTPI and sTPI, we next inquired whether this would be reflected under isothermal conditions, i.e. in the presence of denaturants. We started using the polar but uncharged denaturant urea, which preferentially binds to the denatured state, shifting the equilibrium towards the denatured state (and correspondingly increasing the unfolding kinetics). We performed unfolding experiments by incubating the two proteins in urea solutions of varying concentrations and measured the Trp fluorescence as the ratio between emission at 330 and 350 nm. Furthermore, we also carried out the reverse reaction, i.e.

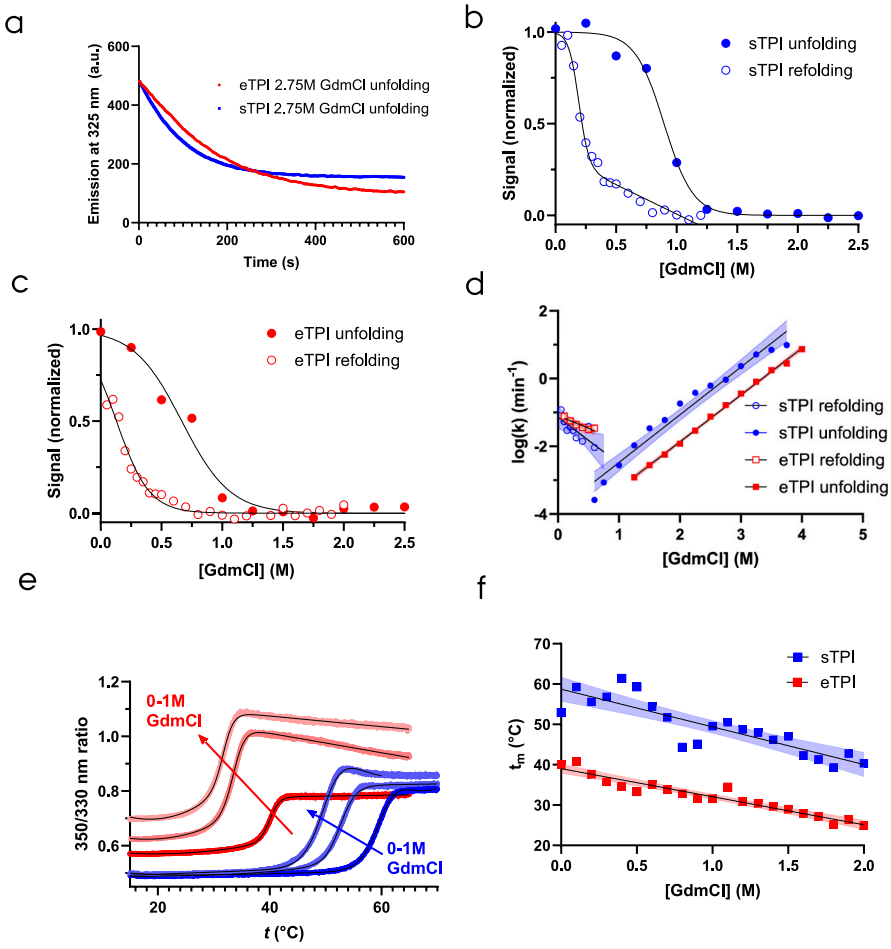

Fig. 3. Effect of GdmCl on TPI stability. **a**: Unfolding kinetics for sTPI (blue) and eTPI (red) in 2.75 m GdmCl, fitted with an exponential decay function. **b**: Unfolding (blue circles) and refolding (empty blue circles) measured by a shift in fluorescence emission from end-point levels of kinetic unfolding and refolding curves. Data fitted with eq. 2. **c**: Unfolding (red squares) and refolding (hollow red squares) equilibrium of eTPI measured by a shift in fluorescence emission. Data are fitted with eq. 2. **d**: Chevron plot for eTPI unfolding (red squares) and refolding (empty red squares), and sTPI unfolding (blue circles) and refolding (hollow blue circles), as a function of GdmCl concentration. Data are fitted with linear regression, of which a semitransparent area fill shows the 95 % confidence interval. **e**: Examples of DSF thermal unfolding in 0-2 M urea fit with eq. 3. **f**: Change in t_m of sTPI (blue circles) and eTPI (red squares) upon titration of GdmCl measured by DSF and fitted with a linear regression where the 95 % confidence intervals are shown as a semitransparent area fill. (For interpretation of the references to colour in this figure legend, the reader is referred to the web version of this article.)

refolding experiments in which the protein was unfolded at high urea concentrations and then transferred to low urea concentrations. The resulting kinetic curves were fitted with a single exponential decay function (see Methods), which yielded endpoint values used for (pseudo-)equilibrium analyses and rate constants for folding and unfolding, k_f and k_u, respectively (a set of time profiles for eTPI between 0 and 4 M urea is shown in Fig. 2a).

For equilibrium analysis, we used endpoint values from the kinetic curves, representing the final state at given conditions of the enzymes. Plotting these values versus denaturant concentration results in sigmoidal curves representing a transition from the folded to the unfolded state which can be fitted with eq. 2. sTPI exhibits a $[den]^{50\%}$, the midpoint of denaturation, of 3.4 ± 0.54 M. However, when we repeated the process in the other direction, starting with the unfolded protein at high urea concentrations (5 M) and then diluting it out to lower concentrations, the endpoint values reached by the end of the exponential decay led to a sigmoidal curve with a significantly lower $[den]^{50\%}$ of 1.3 ± 0.07 M (Fig. 2b). This hysteretic behavior is also shown by eTPI, although not as pronounced since $[den]^{50\%}$ for unfolding is 1.9 ± 0.05 M, and for refolding it is 1.2 ± 0.06 M (Fig. 2c). Notably, the activity of the enzymes was not regained completely upon renaturation from the urea-unfolded state (**Supplementary Fig. S4a**). Hysteresis most likely reflects TPI's dimerization as part of its refolding, a bimolecular reaction which is likely to proceed slowly at low protein concentrations. It is unlikely to involve partial aggregation, since there is sufficient residual denaturant present to suppress aggregation; furthermore, we did not see evidence for protein concentration dependence in refolding experiments (data not shown). In combination with the hysteretic behavior, this data made it clear that neither of the enzymes unfolds reversibly in urea. Therefore, we decided to focus only on the unfolding kinetics in urea, which informs on the kinetic stability of the two enzymes.

A plot of the logarithm of the rate constants versus urea concentration followed a linear correlation for both enzymes. Here, an intersection with the secondary axis at 0 M urea represents the log of unfolding in the buffer, while the slope provides so-called *m*-values. sTPI showed an m_u value of 0.47 ± 0.02 M and a k_u^{water} of 3.9×10^{-6} min^{-1} (Fig. 2d). For eTPI, the m_u value is similar to sTPI, 0.42 ± 0.02 M^{-1}; however, k_u^{water} is 500 times faster than sTPI with a value of 2.1×10^{-3} min^{-1} (Fig. 2d).

We complemented these measurements of kinetic stability by using thermal denaturation with DSF in urea. The resulting curves were sigmoidal but showed an overshoot of signal above t_m, most likely due to aggregation (Fig. 2e). We circumvented the overshoot using a

Table 2
Summary of thermodynamic and kinetic stability parameters for sTPI and eTPI obtained from denaturant-induced unfolding at thermal and isothermal conditions measured by fluorescence or CD.

Conditions	Parameter	eTPI	sTPI
(Pseudo-) equilibrium (urea)	$[urea]^{50\%}_{unfolding}$ [a]	1.9 ± 0.05 M	3.4 ± 0.54 M
	$[urea]^{50\%}_{refolding}$ [a]	1.2 ± 0.06 M	1.3 ± 0.07 M
	$[urea]^{50\%}_{activity}$ [a]	1.6 ± 0.46 M	3.2 ± 0.38 M
(Pseudo-) equilibrium (GdmCl)	$[GdmCl]^{50\%}_{unfolding}$ [a]	0.67 ± 0.06 M	0.90 ± 0.02 M
	$[GdmCl]^{50\%}_{refolding}$ [a]	0.13 ± 0.10 M	0.19 ± 0.02 M
	$[GdmCl]^{50\%}_{activity}$ [a]	NA	NA
Kinetics (urea)	k_u^{water} [b]	2.1×10^{-3} min^{-1}	3.9×10^{-6} min^{-1}
	m_u [b]	0.42 ± 0.02 M^{-1}	0.47 ± 0.02 M^{-1}
Kinetics (GdmCl)	k_u^{water} [b]	2.3×10^{-5} min^{-1}	1.3×10^{-4} min^{-1}
	m_u [b]	1.4 ± 0.02 M^{-1}	1.41 ± 0.1 M^{-1}
Kinetics (urea + NaCl)	k_u^{water} [b]	3.50 ± 0.10 × 10^{-6} min^{-1}	2.64 ± 0.04 × 10^{-6} min^{-1}
	m_u [b]	0.67 ± 0.05 M^{-1}	0.69 ± 0.03 M^{-1}
Equilibrium (urea + heat)	Δt_m [c]	−4.7 ± 0.23 °C/M	−1.7 ± 0.03 °C/M
Equilibrium (GdmCl + heat)	Δt_m [c]	−7.0 ± 0.45 °C/M	−9.4 ± 1.2 °C/M
	ΔC_p [d]	6.0 ± 0.5 kcal/mol	1.6 ± 0.24 kcal/mol
	$\Delta G_{D\text{-}N\ (298\ K)}$ [e]	5.5 ± 0.4 kcal/mol	11.2 ± 0.6 kcal/mol
	$m_{D\text{-}N}$ [e]	3.2 ± 0.50 M^{-1}	2.6 ± 0.39 M^{-1}

Notes:
[a] Midpoint of denaturation in urea (data in Fig. 2b and c) and GdmCl (data in Figs. 3b and 2c) calculated using eq. 2 measured by fluorescence endpoints.
[b] Unfolding rate in water found by extrapolation of k_u values to 0 M urea (data in Fig. 2d) or GdmCl (data Fig. 3d) measured by fluorescence kinetics. The *m*-values are found as the slope of the linear regression.
[c] Change in the midpoint of thermal unfolding as a function of urea (data in Fig. 2f) and GdmCl (data in Fig. 3f) found by fitting DSF data to eq. 3, as shown by examples in Figs. 2e and 3e.
[d] Calculated as a slope of the linear regression of the relationship between ΔH_{Tm} and T_m at 0–3 M GdmCl measured by DSF. Data is shown in Fig. 4a. d.
[e] Found by extrapolation of values $\Delta G_{D\text{-}N\ (298\ K)}$ in 0–3 M GdmCl found in Fig. 4b were calculated using eq. 4 to 0 M GdmCl. The *m*-values are found as the slope of the linear regression.

polynomial component to the baseline (eq. 3). A plot of t_m versus [urea] revealed that eTPI is significantly more sensitive to urea than sTPI, with a decline in t_m of 4.7 ± 0.23 °C/M for eTPI compared to 1.7 °C/M ± 0.03 for sTPI (Fig. 2f). We also plotted ΔH_{Tm} versus T_m (**Supplementary Fig. S5**), where the slope corresponds to the heat capacity of unfolding, ΔC_p. Surprisingly, for both proteins, we observe a negative linear correlation between T_m and ΔH_{Tm} giving ΔC_p values of −2.1 ± 0.51 kcal/mol for sTPI and − 2.9 ± 0.41 kcal/mol for eTPI. A negative ΔC_p value (i.e. a *decrease* in heat capacity as the protein unfolds) is predicted to stabilize the protein as the temperature increases according to eq. 3, which is obviously contrary to the observed thermal unfolding of both proteins and very difficult to rationalize; it is most likely an artefact of the data analysis. Conventionally positive ΔC_p values are normally obtained from thermal denaturation data obtained over a range of denaturant concentrations [41,42].

3.3. Guanidinium chloride cancels the difference in unfolding kinetics between sTPI and eTPI observed in urea

Given the significant hysteresis of TPI unfolding in urea and the anomalous ΔC_p values observed from our analysis, we turned to the more potent denaturant guanidinium chloride (GdmCl), which we previously showed to lead to reversible two-state unfolding of the kinetically stable outer membrane protein OmpA [43], removing hysteresis behavior of OmpA in urea. We utilized the same approach to data analysis as with urea, where kinetic experiments were fitted with an exponential decay function, which provided kinetic constants and endpoint values (Fig. 3a). However, plotting the endpoint values of the kinetic experiments reveals sigmoidal curves that again show marked hysteresis between unfolding and refolding, similar to urea. Here, we saw that sTPI unfolding has a $[GdmCl]^{50\%}$ value of 0.90 ± 0.02 M, while that for refolding was calculated to 0.19 ± 0.02 M and had a more complex two-phase profile (Fig. 3b). Similarly, low values were observed for eTPI, where $[GdmCl]^{50\%}$ for unfolding was 0.67 ± 0.06 M and refolding 0.13 ± 0.1 M (Fig. 3c). Activity was only partially regained upon refolding (**Supplementary Fig. S4b**). Once again, the lack of microscopic reversibility likely reflects the slow process of dimerization. Accordingly, we decided only to focus on the unfolding step. Plotting the log of the kinetic rate constants versus [GdmCl] led to $m_u = 1.41 \pm 0.1\ M^{-1}$ and k_u^{water} of $1.3 \times 10^{-4}\ min^{-1}$ for sTPI, and eTPI unfolding parameters were $m_u = 1.4 \pm 0.02\ M^{-1}$ and k_u^{water} of $2.3 \times 10^{-5}\ min^{-1}$ (Fig. 3d). GdmCl-based data predict that sTPI unfolds 5-fold faster than eTPI in water, a 2500-fold change in relative unfolding rates compared to urea data which extrapolate to a 500-fold faster unfolding of eTPI than sTPI in water. The unfolding parameters are summarized in Table 2.

Thermal unfolding of both enzymes in the presence of 0–3 M GdmCl led to a systematic decrease in t_m with increasing [GdmCl], similar to urea (Fig. 3e). In contrast to urea, GdmCl decreases the t_m of sTPI more steeply than that of eTPI with slopes of −9.4 ± 1.2 °C/M and − 7.0 ± 0.45 °C/M, respectively (Fig. 3f). Furthermore, we see a conventional increase in ΔH_{Tm} with T_m, leading to positive ΔC_p values of 1.6 ± 0.24 and 6.0 ± 0.5 kcal/mol for sTPI and eTPI, respectively (Fig. 4a). Eq. 4 provided $\Delta G_{D\text{-}N}$ at 25 °C for both enzymes as a function of [GdmCl] (Fig. 4b) as well as $m_{D\text{-}N}$-values for denaturation, which were 3.2 ± 0.5 M^{-1} for sTPI and 2.6 ± 0.39 M^{-1} for eTPI (Fig. 4b). Although these values are not significantly different from each other due to the relatively large standard errors, they reproduce the trend from urea denaturation data that sTPI shows a larger *m*-value for unfolding in denaturant. Furthermore, the ΔC_p values combined with the measured ΔH_{Tm} values at 25 °C allow us to calculate $\Delta G_{D\text{-}N}$ as a function of temperature using eq. 3 for both eTPI and sTPI (**Fig. 4cd**). When combined with measurements of initial velocity at these temperatures, we see that the drop in activity coincides nicely with the loss of native structure as $\Delta G_{D\text{-}N}$ reaches zero and below.

3.4. Electrostatic interactions may explain part of the difference between the action of urea and GdmCl on eTPI and sTPI

sTPI is far more resistant towards denaturation than eTPI in urea, based on equilibrium data ($[urea]^{50\%}$), kinetics (k_u^{water}), and shift in melting temperature (Δt_m). However, in GdmCl the two enzymes show a similar $[GdmCl]^{50\%}$ and sTPI unfolds faster than eTPI. A major difference between urea and GdmCl is that the former is a polar molecule, and the latter is a salt. We hypothesized that the ionic strength of the solution might explain the difference in the effects of the two denaturants, so we investigated the effect of NaCl on the activity and stability of both enzymes. Interestingly, the activities of sTPI and eTPI are equally impaired by NaCl, and only approx. 25 % of the original activity is observed at 500 mM NaCl in both cases (Fig. 5a). We also tested the thermal stability of both enzymes in the presence of NaCl using DSF. Here, we observed that the t_m of eTPI increases by 9.5 °C as we go from <100 mM to 4 M NaCl, while the t_m of sTPI is almost independent of salt and shifts slightly downwards by 0.7 °C in the same concentration range (Fig. 5b). Thus, eTPI is significantly stabilized by NaCl (possibly by screening effects) while sTPI is marginally destabilized.

To mimic possible screening effects by the guanidinium and chloride ions, we measured the unfolding of the proteins in urea with equimolar amounts of NaCl. The experiments were performed similarly to the urea and GdmCl experiments, where we measured the kinetics rates and endpoints of unfolding by Trp fluorescence. We observe that NaCl

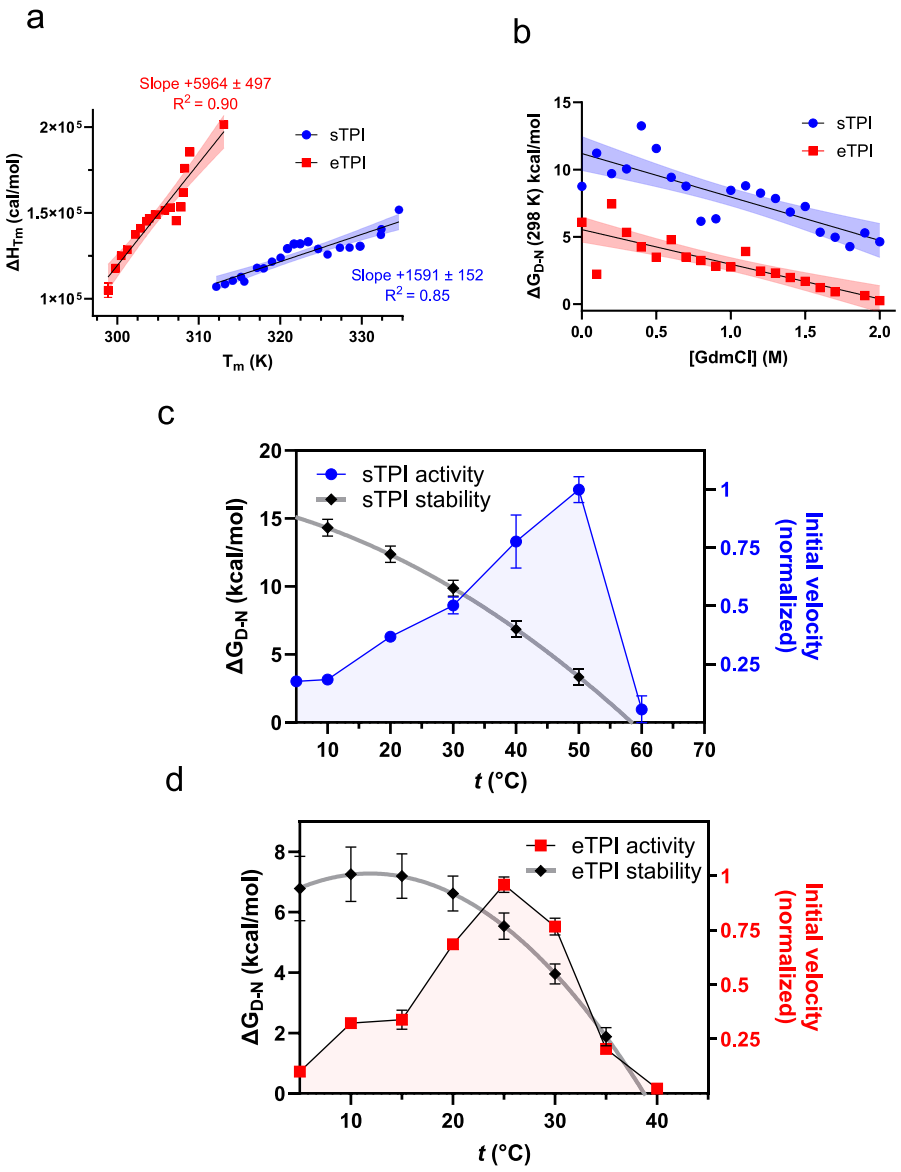

Fig. 4. **a**: ΔH_{Tm} as a function of melting temperature of sTPI (blue circles) and eTPI (red squares) in 0–3 M GdmCl, obtained from DSF thermal scans fit to eq. 3. The resulting data are fit to linear regression, where ΔC_p is found as the slope, and the 95 % confidence interval is shown as a semitransparent area fill. **b**: $\Delta G_{D\text{-}N}$ at 298 K of sTPI (blue circles) and eTPI red squares) calculated using ΔH_{Tm} and T_m values measured by DSF using values for ΔC_p obtained as the slopes in Fig. 4a. **c**: $\Delta G_{D\text{-}N}$ as a function of temperature for sTPI (black diamond) fit to a second-order polynomial function compared to the activity profile (blue circles) **d**: $\Delta G_{D\text{-}N}$ as a function of temperature for sTPI (black diamond) fit to a second-order polynomial function and compared to the activity profile (red squares). (For interpretation of the references to colour in this figure legend, the reader is referred to the web version of this article.)

stabilizes eTPI, as $[urea]^{50\%}$ is shifted from 1.9 ± 0.05 M to 2.5 ± 0.06 M (Fig. 2c and 5c). In striking contrast, denaturation of sTPI shifts $[urea]^{50\%}$ from 3.4 ± 0.54 M without NaCl to 2.0 ± 0.01 M in the presence of NaCl (Fig. 2b and 5c). Interestingly, the kinetic analysis showed almost identical k_u^{water} values, namely 3.5×10^{-6} min^{-1} for eTPI and 2.6×10^{-6} min^{-1} for eTPI (Fig. 5d). Furthermore, the m_u-values are very similar (0.67 ± 0.05 M^{-1} and 0.69 ± 0.03 M^{-1} for eTPI and sTPI, respectively). Thus, an equimolar amount of NaCl in urea to some degree equalizes thermodynamic stability between the two enzymes.

3.5. *Crystal structures reveal that sTPI dimerization involves more hydrophobic interactions than eTPI*

To provide the basis for a more detailed structural comparison of the two proteins, we determined crystal structures of eTPI and sTPI at 1.85 and 1.5 Å resolution, respectively (see Table 3 for crystallographic data statistics). The model of eTPI (9QUU) includes residues 2–257 (of 261) while that of sTPI (9QUS) covers residues 1–273 (of 273) for both subunits. The structures are similar, with a root mean square deviations of 2.08 Å for all main chain atoms. Both enzymes assume the classical TPI $(\beta\alpha)_8$-fold, where eight α-helices surround the eight-stranded β-sheet TIM barrel core that contains the active site (Fig. 6a). The catalytic residues (His 98 and Glu 170 in sTPI and His 100 and Glu 172 in eTPI) are well conserved between the two enzymes with no apparent differences (Fig. 6b). Notably, the loop that covers the active site is in the open position for eTPI and closed position for sTPI (Fig. 6b, **arrows**). The divergence in loop orientation is probably due to different crystal packing. A similar difference has been observed for the same TPIs with different ligands bound [23,44–46]. Two notable substitutions near the active site involve an absence of aromatic residues in eTPI, as Tyr 104 and Phe 105 in sTPI are altered to Leu 106 and His 107 in eTPI (Fig. 6c). These amino acids constitute a bridge between the subunit interface and

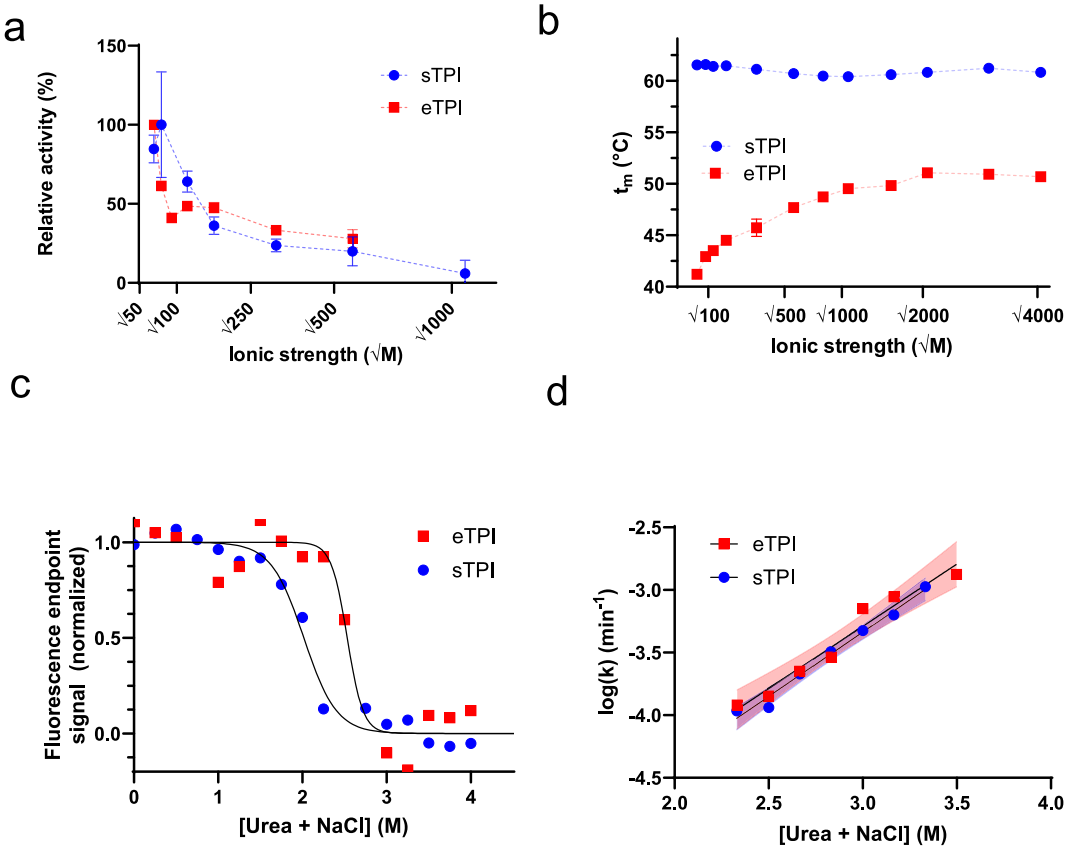

Fig. 5. Effect of NaCl on TPI stability and unfolding kinetics. **a**: Activity of TPI (blue circles) and eTPI (red squares) measured as initial velocity as a function of ionic strength using different concentrations of NaCl. **b**: Thermal stability of sTPI (blue circles) and eTPI (red squares) represented by t_m measured by DSF as a function of ionic strength using different concentrations of NaCl. **c**: Isothermal unfolding of sTPI (blue circles) and eTPI (red squares) in urea with an equimolar amount of NaCl measured by 330/350 shift in fluorescence endpoints. Data fitted to the eq. 2. **d**: Log of unfolding kinetics rate constants of sTPI (blue) and eTPI (red) as a function of urea with an equimolar amount of NaCl measured by a shift in fluorescence emission. The data are fit to a linear regression where the 95 % confidence intervals are shown as a semitransparent area fill. (For interpretation of the references to colour in this figure legend, the reader is referred to the web version of this article.)

the active site. Proteolytic nicking in this spot will lead to a ~16 kDa fragment. A band of that size is indeed observed by the ProtK assay (**Supplementary Fig. S2**).

Assembly analysis of both structures using PDBePISA [34] shows that both proteins are able to assemble into stable homodimers [47,48]. PDBePISA predicts that the solvation free energy of folding (ΔG_{solv}) of individual monomer units is very similar for the two proteins, 229.5 kcal/mol for eTPI and 227.8 kcal/mol for sTPI (Table 4). However, based on interface hydrophobicity, the free energy gain upon dimerization (ΔG^{int}_{solv}) is predicted to be −24.0 kcal/mol for eTPI and − 29.0 kcal/mol for sTPI (Table 4) despite having almost identical interface area. That is, sTPI is predicted to dimerize more strongly than eTPI. Interestingly, the interface of the eTPI dimer has 26 potential hydrogen bonds, whereas the sTPI interface only has 16, suggesting that the association of the sTPI dimer is driven more by hydrophobic interactions than eTPI. Furthermore, sTPI has two symmetric salt bridges in the critical surface area of the interfacing subunits (Fig. 6d), which might explain the strong unfolding effect of the charged GdmCl compared to the uncharged urea. Calculation of the surface electrostatics using APBS Electrostatics shows that eTPI has a significantly more negative electrostatic potential, which is particularly pronounced in the dimerization interface (Fig. 6e). Interestingly, the eTPI catalytic pocket also has a more positive surface potential, however, we did not observe significant differences in activity as a function of NaCl concentration.

3.6. Modest stabilization of eTPI by EVE-based substitutions

We performed in silico prediction of high evolutionary fitness of eTPI to improve the stability and activity of the enzyme. To design variants of eTPI with improved stability and activity, we utilized a deep learning model called "EVE" (Evolutionary model of Variant Effect), which predicts the effects of protein variants based on evolutionary sequence information [37]. EVE models the natural distribution of protein sequences observed across organisms using a Bayesian Variational Autoencoder (VAE), capturing the evolutionary constraints on protein sequences that maintain fitness. By modeling this distribution, EVE implicitly learns an internal representation of protein architecture and function, enabling the prediction of the effects of mutations on protein stability and activity. From the EVE predictions, we selected mutations that have the highest fitness score. Four single-mutation variants (L106Y, N137Y, S186A, and K200A) and a quadruple mutant (QM) combining all these four mutations were made and tested experimentally to verify their stability and activity. The mutated residues are highlighted in red in **Supplementary Fig. S6**. Interestingly, three of the four best-scoring substitutions involve changes to residues which are already found in the equivalent positions in sTPI.

All variants expressed well (approx. 25 mg yield per L bacterial culture). None of the mutations had detrimental effects on activity (Fig. 7a), and each single mutation provided small improvements in stability (Fig. 7b). The QM exhibited a more substantial increase in melting temperature by 2–3 °C across various urea concentrations in an additive fashion. Consistent with QM's significant increase in stability, WT and QM at 45 °C unfold with $t_{½}$ values of of 8.4 ± 1.2 and 12.1 ± 0.2 s, respectively (Fig. 7c). In conclusion, our study illustrates positive epistasis where the combination of mutations in the QM variant led to greater improvements in stability than any single mutation alone.

Table 3
Data collection and refinement statistics. Numbers in parentheses represent the outermost resolution shell.

	eTPI (9QUU)	sTPI (9QUS)
Wavelength (Å)	0.97623	0.97623
Resolution range (Å)	47.62–1.634 (1.68–1.63)	49.01–1.461 (1.48–1.46)
Space group	$P4_32_12$	$P2_12_12_1$
Unit cell (a, b, c, Å) (α, β, γ, degrees)	86.102, 86.102, 152.835 90, 90, 90	47.751, 47.796, 196.022 90, 90, 90,
Total reflections	1,410,965 (9619)	715,444 (16319)
Unique reflections	69,600 (3425)	78,240 (2261)
Multiplicity	20.3 (2.8)	9.1 (7.2)
Completeness (%)	87.09 (2.68)	99.06 (89.12)
Mean I/sigma(I)	14.20 (0.09)	21.63 (0.94)
Wilson B-factor (Å^2)	9.25	20.99
R_{merge}	0.09135 (7.767)	0.05237 (1.649)
R_{meas}	0.09347 (9.223)	0.05549 (1.779)
R_{pim}	0.01931 (4.848)	0.01799 (0.6468)
$CC_{1/2}$	1 (0.0257)	0.999 (0.615)
CC*	1 (0.224)	1 (0.873)
Reflections used in refinement	62,560 (146)	78,225 (2285)
Reflections used for R_{free}	1803 (3)	0 (0)
R_{work}	0.1882 (0.9826)	0.1675 (0.3358)
R_{free}	0.2038 (0.9772)	0.1983 (0.3568)
Number of non-hydrogen atoms	4107	4136
macromolecules	3765	3850
ligands	7	0
solvent	335	286
Protein residues	514	506
rms bonds	0.003	0.004
rms angles	0.55	0.81
Ramachandran favored (%)	97.65	96.02
Ramachandran allowed (%)	1.96	3.59
Ramachandran outliers (%)	0.39	0.4
Rotamer outliers (%)	0.26	0.49
Clashscore	3.03	2.74
Average B-factors (Å^2)	47	18.4
macromolecules	46.7	18.09
ligands	60.98	
solvent	50.11	22.47

Nevertheless, we note that the thermal stability of the QM mutant of eTPI is still significantly lower than that of sTPI with t_m values of 47.3 °C versus 64 °C.

4. Discussion

4.1. Enzymes from cold-active organisms can be active at higher temperatures

This study aimed to compare and contrast the stability profiles of two related household enzymes from two bacteria with distinct low-temperature profiles. We reasoned that the organisms' temperature profiles could be reflected in the thermal stabilities of their associated enzymes. However, this is obviously very simplistic. An organism's optimal growth temperature is determined by the overall performance of multiple different enzymes; in fact, Picotti and co-workers have shown that growth collapse is governed by the denaturation of a small number of critical hub proteins which interact metabolically with a large number of other partner proteins [24]. Thus, in practice, an optimal growth temperature only limits individual enzymes' thermal stability. Indeed, using a quenched coupled activity assay, we observed that sTPI is active over a broad temperature range with a high t_{opt} of 50 °C. sTPI is from a stenopsychrophilic organism, *R. psychrophilum*, which does not grow above 22 °C [5], indicating that the enzyme functions well beyond its host organism's normal growth temperature. On the other hand, eTPI from the eurypsuchrophilic *Rhodococcus* sp. *JG-3* showed a low t_{opt} at 25 °C, which fits the bacteria's maximal growth temperature of 30 °C [4]. Thus, sTPI seems to follow the overall limitation in stability set by its host organism, while eTPI performs well beyond the minimal requirements. Nevertheless, the clear difference in thermal stability between the two enzymes provides an opportunity to compare properties and obtain additional insights into the basis for low-temperature activity.

4.2. Loss of activity before loss of structure is seen for both proteins

Thermal denaturation of both enzymes measured by either far- and near UV CD or DSF showed that their optimal activity temperature is well below their denaturation temperatures, that is, they lose activity well before they lose global structure. This discrepancy, which is particularly clear for eTPI, is a typical feature of psychrophilic enzymes and has traditionally been ascribed to the local loss of structure around the active site. The phenomenon correlation may extend beyond psychrophilic enzymes since similar results have been observed for TPI from the mesophilic fungus *F. oxisporum* with a t_{opt} of 40 °C and t_m of 51.4 °C [49]. We introduced the proteinase K (PK) degradation assay as a convenient way to probe protein flexibility. This showed that cleavage of both enzymes follows a sigmoidal curve whose midpoint temperature is only 2–5 °C above t_{opt}. For sTPI, t_{ProtK} is ~7 °C below the structural denaturation temperature t_m of ca. 64 °C. We would generally expect t_{ProtK} to be somewhat lower than t_m, since proteinase K will irreversibly cleave whatever small fraction of unfolded protein is present in the solution, thus amplifying the extent of denaturation. However, in the case of eTPI, the difference between t_{ProtK} and t_m is so large (~13 °C) that there is likely local unfolding that is not detected by spectrophotometric methods. This identifies eTPI as a more typical psychrophilic enzyme than sTPI, consistent with its general lower stability. Consistent with this, heat-induced unfolding kinetics experiments show that eTPI has a significantly lower $\Delta G^{\ddagger}$ unfolding value than sTPI.

4.3. Electrostatics has a profound influence on eTPI and sTPI stability

We utilized equilibrium and kinetic approaches to measure thermal and chemical denaturation. Both enzymes unfold in a sigmoidal, two-state manner but sTPI is far more resistant towards unfolding towards urea than eTPI. Interestingly, both enzymes exhibited hysteretic refolding behavior with very similar refolding midpoints around 1.25 M urea. These values were calculated from endpoint values in the kinetic experiments reflecting the plateau values from exponential decay and, thus, apparent equilibrium states. The hysteresis likely occurs because the exponential decays from unfolding and refolding experiments derive from different folding/unfolding pathways. The structural state reached under refolding conditions does not represent a properly folded native and enzymatically active state but rather a partially refolded species that does not attain the folded state within the experiment's lifetime, likely due to the requirement for dimerization which is a slow bimolecular process.

sTPI unfolds almost showed three orders of magnitude more slowly than eTPI, which may be partly due to urea having a different impact on the two enzymes. We attempted to determine the stability of the TPIs in urea by performing DSF thermal unfolding experiments in 0–3 M but could observe anomalous negative ΔC_p values, which could not be used for thermodynamic stability determination. This is no artefact caused by our second-order polynomial baseline in eq. 3, since fitting with a more conventional linear baseline for the unfolded state (eq. 1) did not alter this anomaly (data not shown). We also note that the t_m of eTPI decreased 2.7 times more when comparing the -1.7 ± 0.03 °C/M slope to the -4.7 ± 0.23 °C/M of sTPI, showing that sTPI is less affected by urea than eTPI.

Given the significant differences in unfolding in urea, we were surprised to see that the two enzymes have comparable stability in GdmCl, once again accompanied by hysteretic behavior with comparable refolding values, as well as very similar kinetic unfolding rates. DSF data for thermal denaturation in GdmCl provided a conventional positive

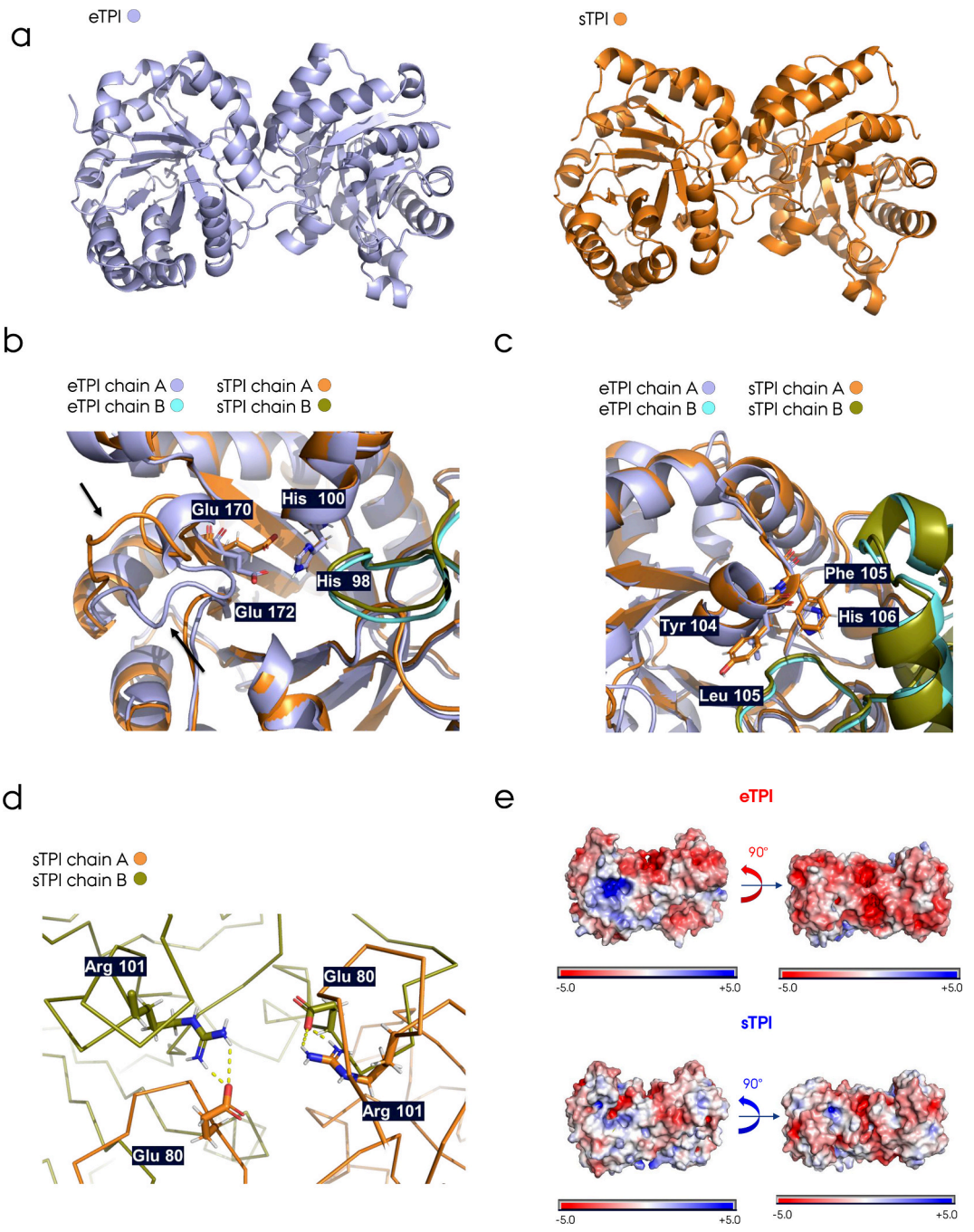

Fig. 6. Crystal structures of eTPI and sTPI. **a**: Structure of eTPI (9QUU) (left, purple) and sTPI (9QUS) (right, orange) shown in cartoon form. **b**: The active site including catalytic residues of eTPI (Glu 170 and His 100) and sTPI (Glu 172 and His 98). The loop of the neighboring subunit is shown in cyan and green for eTPI and sTPI, respectively. The arrows indicate the mobile loop covering the active site. **c**: Amino acid residues in eTPI (Leu 105 and His 106) and sTPI (Tyr 104 and Phe 105) that bridge the interface of the subunits with the catalytic cleft. **d**: Salt bridges in sTPI consisting of Glu 80 and Arg 101 at the subunit interface. **e**: Surface electrostatics of eTPI (left) and sTPI (right) calculated using ABPS Electrostatics [53] seen from two perspectives. Red and blue grading represents negative and positive surface potential, respectively. (For interpretation of the references to colour in this figure legend, the reader is referred to the web version of this article.)

heat capacity of unfolding, but with the extra "twist" that the two proteins differ significantly in heat capacity. According to Pace and Scholtz [50], the heat capacity of a protein can be roughly estimated as 12 cal/mol/K/residue which for these two proteins yields around 6.7 kcal/mol/K. While this corresponds very well to eTPI's measured heat capacity value (6.0 ± 0.5 kcal/mol/K), it severely overestimates that of sTPI which is measured to 1.6 ± 0.5 0.24 kcal/mol/K. Based on these ΔC_p values, we find that sTPI is the most stable and the temperature-dependence of the two enzymes leads to melting temperatures (from inspection of the temperature where $\Delta G_{D\text{-}N}$ is 0) of 58.4 °C for sTPI and 38.7 °C for eTPI, both reasonably close to the recorded t_m values by far- and near-UV and DSF. Interestingly, the ProtK assay showed sTPI to have a midpoint of transition at 55.8 °C, which is only 2.6 °C below the predicted t_m from the GdmCl DSF experiments. On the other hand, eTPI had a $ProtK_{50\%}$ at 26.9 °C, which is 11.8 °C below the t_m predicted by the thermal unfolding with GdmCl. This discrepancy suggests that the activity loss of eTPI (which has a more pronounced psychrophilic character) upon thermal unfolding is caused by local unfolding, whereas sTPI, to a greater degree, loses activity upon global unfolding.

The overall picture that emerges is that sTPI is significantly more

Table 4
Results from PDBePISA analysis obtained by input of sTPI and eTPI structures.

	sTPI	eTPI
ΔG_{solv} (kcal/mol) [a]	227.8	229.5
ΔG^{int}_{solv} (kcal/mol) [b]	−29.0	−24.0
Interface area (Å^2) [c]	1678.8	1654.8

Notes:
[a] ΔG_{solv} indicates the solvation free energy of folding for the corresponding structure, in kcal/mol.
[b] ΔG^{int}_{solv} represents solvation energy gain (kcal/mol) from interface formation, calculated as the solvation energy difference between isolated and interfacing structures. Negative value suggests a hydrophobic interface or strong protein affinity, excluding effects of hydrogen bonds and salt bridges.
[c] Interface area in Å^2, calculated as half the difference between the total accessible surface areas of the isolated and interacting structures.

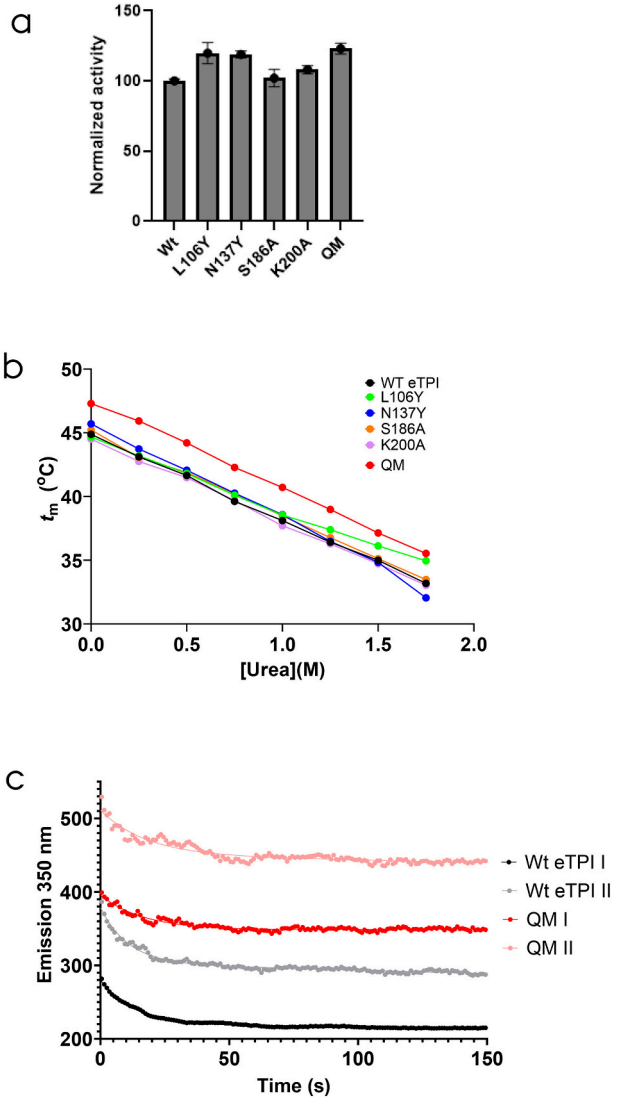

Fig. 7. Activity and stability of the 4 individual mutants of eTPI and their combined effects in the quadruple mutant QM. **a.** The mutations do not decrease the activity of eTPI. **b.** t_m values obtained from DSF experiments between 0 and 1.75 M urea show a cumulative effect in the QM mutant compared to the individual mutants. **c.** The unfolding kinetics of QM at 45 °C are slightly slower than for WT eTPI (half times of 12.1 versus 8.4 s).

thermally stable (at least in the absence of confounding electrostatic factors) and that its unfolding pathway involves a much more substantial activation barrier, both seen as generally slower kinetics and as a different type of dependence on chemical denaturants. However, the marked divergence between the rate constants of unfolding of the two enzymes in water which emerge from extrapolation of three different sets of experiments (based on urea, GdmCl and urea + NaCl) indicate that linear extrapolation from the measured concentration range is not valid and that the relationship between the log of unfolding and denaturant concentration changes at low denaturant concentrations. This may reflect complex phenomena such as moving transition states [51] or changes in denaturant activity [52], which is beyond the scope of the current study.

GdmCl is chemically closely related to urea with a third amino group instead of the carbonyl found in urea. The amino group makes GdmCl strongly basic and positively charged at neutral pH. We investigated whether the particularly large difference in stability and folding kinetics of sTPI may be due to the ionic strength of the GdmCl solutions. Unfolding the enzymes by heat in the presence of sodium chloride had a very different effect. Where eTPI was strongly stabilized by titration of NaCl, it had a slightly destabilizing effect on sTPI. Interestingly, both enzymes were similarly inhibited by NaCl in terms of activity. Kinetic measurements of unfolding in urea with equimolar amounts of NaCl showed similar results to the DSF experiments, where eTPI was stabilized while sTPI stability was lowered. Calculating the surface electrostatic potential revealed that eTPI has a significantly more negatively charged surface than sTPI (Fig. 6e). In particular, the interface between the eTPI subunits is negatively polarized, which is best seen by the top view of the eTPI electrostatic potential map (second map from the left). This suggests that eTPI subunits may to some degree repel each other, unless stabilized by salt ions. This repulsion could explain eTPI's lower stability and why increased ionic strength stabilizes the protein.

4.4. Structural differences

The determined crystal structures of eTPI and sTPI showed that both enzymes share the same classical $(\beta\alpha)_8$-fold (TIM barrel) known among TPIs. However, although the active site is perfectly conserved, there are differences in the vicinity, most notably the bridging residues between the interface and the active site. Furthermore, computational analysis of the structure revealed that although the monomeric structures are predicted to have similar solvation stabilities, sTPI is stabilized by dimerization to a greater extent.

5. Concluding remarks

The comparatively low stability of sTPI in GdmCl compared to urea combined with the ability of sodium chloride to recapitulate this effect implies that electrostatic interactions play a prominent role in stabilizing the stenopsychrophilic sTPI compared to its eurypsychrophilic counterpart eTPI. Our study demonstrates the utility of evolutionary information-based machine learning model in protein engineering. By leveraging the rich information embedded in natural sequence variation, we can predict mutations that enhance both the stability and activity of enzymes, although the increase in stability only represents a small fraction of the stability differences between the two proteins. Nevertheless, we observed positive epistasis between the mutations, where the combination of mutations in the QM variant led to greater improvements in stability than any single mutation alone. This synergistic effect underscores the potential of combining multiple beneficial mutations to achieve enhanced enzyme properties.

CRediT authorship contribution statement

Jan S. Nowak: Writing – original draft, Methodology, Investigation, Formal analysis, Conceptualization. **Sune Olesen:** Writing – original

draft, Investigation. **Pengfei Tian:** Methodology, Investigation, Formal analysis. **René L. Bærentsen:** Investigation. **Ditlev E. Brodersen:** Writing – review & editing, Supervision, Investigation, Formal analysis. **Daniel E. Otzen:** Writing – review & editing, Writing – original draft, Supervision, Project administration, Methodology, Investigation, Funding acquisition, Formal analysis, Conceptualization.

Declaration of competing interest

The authors declare that they have no known competing financial interests or personal relationships that could have appeared to influence the work reported in this paper.

Acknowledgements

We are grateful for support from Independent Research Foundation Denmark | Technology and Production (grant 9041-00123B) to D.E.O and for inspiring discussions on psychrophilicity with collaborators Mariane Thøgersen and Peter Stougaard. We thank Malthe Kjær Bendtsen, Elia Viezzi, Nikoline Kruuse, Julie Astono, Rune Efferbach Toft and Alexander Højlund Toftgaard for constructive input on psychrophilic enzymes. R. L. B. and D. E. B. were supported by grants from the Novo Nordisk Foundation (NNF17OC0028072 and NNF18OC00306463).

Appendix A. Supplementary data

Supplementary data to this article can be found online at https://doi.org/10.1016/j.bbapap.2025.141072.

Data availability

Data will be made available on request.

References

[1] S. D'Amico, T. Collins, J.C. Marx, G. Feller, C. Gerday, C. Gerday, Psychrophilic microorganisms: challenges for life, EMBO Rep. 7 (4) (2006) 385–389.
[2] R. Cavicchioli, K.S. Siddiqui, Cold-adapted enzymes, in: A. Pandey, C. Webb, C. R. Soccol, C. Larroche (Eds.), Enzyme Technology, Springer, New York, New York, NY, 2006, pp. 615–638.
[3] C. Bakermans, P.W. Bergholz, D.F. Rodrigues, T.A. Vishnivetskaya, H.L. Ayala-del-Río, J.M. Tiedje, Genomic and expression analyses of cold-adapted microorganisms, Polar Microbiol. (2011) 126–155.
[4] J. Goordial, I. Raymond-Bouchard, J. Ronholm, N. Shapiro, T. Woyke, L. Whyte, C. Bakermans, Improved-high-quality draft genome sequence of Rhodococcus sp. JG-3, a eurypsychrophilic Actinobacteria from Antarctic Dry Valley permafrost, Stand. Genomic Sci. 10 (1) (2015).
[5] M. Schmidt, A. Priemé, P. Stougaard, Rhodonellum psychrophilum gen. nov., sp. nov., a novel psychrophilic and alkaliphilic bacterium of the phylum Bacteroidetes isolated from Greenland, Int. J. Syst. Evol. Microbiol. 56 (12) (2006) 2887–2892.
[6] G. Feller, Psychrophilic enzymes: from folding to function and biotechnology, Scientifica 2013 (2013) 1–28.
[7] G. Feller, Protein stability and enzyme activity at extreme biological temperatures, J. Phys. Condens. Matter 22 (32) (2010) 323101.
[8] S. D'Amico, J.-C. Marx, C. Gerday, G. Feller, Activity-stability relationships in extremophilic enzymes, J. Biol. Chem. 278 (10) (2003) 7891–7896.
[9] G. Feller, D. d'Amic, C. Gerday, Thermodynamic stability of a cold-active α-amylase from the Antarctic Bacterium Alteromonas haloplanctis, Biochemistry 38 (14) (1999) 4613–4619.
[10] J. Sočan, M. Purg, J. Åqvist, Computer simulations explain the anomalous temperature optimum in a cold-adapted enzyme, Nat. Commun. 11 (1) (2020) 2644.
[11] S. Joshi, T. Satyanarayana, Biotechnology of cold-active proteases, Biology (Basel) 2 (2) (2013) 755–783.
[12] J.G. Hjörleifsson, B. Ásgeirsson, Cold-active alkaline phosphatase is irreversibly transformed into an inactive dimer by low urea concentrations, Biochim. Biophys. Acta 1864 (7) (2016) 755–765.
[13] K.S. Siddiqui, R. Cavicchioli, Cold-adapted enzymes, Annu. Rev. Biochem. 75 (2006) 403–433.
[14] G. Feller, C. Gerday, Psychrophilic enzymes: hot topics in cold adaptation, Nat. Rev. Microbiol. 1 (3) (2003) 200–208.
[15] J. Åqvist, Cold adaptation of triosephosphate isomerase, Biochemistry 56 (32) (2017) 4169–4176.
[16] S. Robin, D.M. Togashi, A.G. Ryder, J.G. Wall, Trigger factor from the psychrophilic bacterium Psychrobacter frigidicola is a monomeric chaperone, J. Bacteriol. 191 (4) (2009) 1162–1168.
[17] M. Rutkiewicz, A. Bujacz, G. Bujacz, Structural features of cold-adapted dimeric GH2 β-D-galactosidase from Arthrobacter sp. 32cB, Biochim. Biophys. Acta, Proteins Proteomics 1867 (9) (2019) 776–786.
[18] K.S. Siddiqui, G. Feller, S. D'Amico, C. Gerday, L. Giaquinto, R. Cavicchioli, The active site is the least stable structure in the unfolding pathway of a multidomain cold-adapted α-amylase, J. Bacteriol. 187 (17) (2005) 6197–6205.
[19] T. Collins, M.-A. Meuwis, C. Gerday, G. Feller, Activity, stability and flexibility in glycosidases adapted to extreme thermal environments, J. Mol. Biol. 328 (2) (2003) 419–428.
[20] J.K. Hobbs, W. Jiao, A.D. Easter, E.J. Parker, L.A. Schipper, V.L. Arcus, Change in heat capacity for enzyme catalysis determines temperature dependence of enzyme catalyzed rates, ACS Chem. Biol. 8 (11) (2013) 2388–2393.
[21] J. Sočan, M. Purg, J. Åqvist, Computer simulations explain the anomalous temperature optimum in a cold-adapted enzyme, Nat. Commun. 11 (1) (2020).
[22] G. Finne, J.R. Matches, J. Liston, A comparative study on the heat stability of triosephosphate isomerase in psychrophilic, psychrotrophic, and mesophilic clostridia, Can. J. Microbiol. 21 (11) (1975) 1719–1723.
[23] M. Alvarez, J.P. Zeelen, V. Mainfroid, F. Rentier-Delrue, J.A. Martial, L. Wyns, D. Maes, et al., Triose-phosphate isomerase (TIM) of the psychrophilic BacteriumVibrio marinus: kinetic and structural properties*, J. Biol. Chem. 273 (4) (1998) 2199–2206.
[24] P. Leuenberger, S. Ganscha, A. Kahraman, V. Cappelletti, P.J. Boersema, C. von Mering, , et al.P. Picotti, Cell-wide analysis of protein thermal unfolding reveals determinants of thermostability, Science 355 (6327) (2017).
[25] N.J. Greenfield, Using circular dichroism collected as a function of temperature to determine the thermodynamics of protein unfolding and binding interactions, Nat. Protoc. 1 (6) (2006) 2527–2535.
[26] A. Fersht, U.A. Fersht, W.H. Freeman, Company, Structure and Mechanism in Protein Science: A Guide to Enzyme Catalysis and Protein Folding, W. H. Freeman, 1999.
[27] A.R. Fersht, Structure and mechanism in protein science, in: A Guide to Enzyme Catalysis and Protein Folding, Freeman & Co, New York, 1999.
[28] H. Walden, G.S. Bell, R.J.M. Russell, B. Siebers, R. Hensel, G.L. Taylor, Tiny TIM: a small, tetrameric, hyperthermostable triosephosphate isomerase11Edited by R. Huber, J. Mol. Biol. 306 (4) (2001) 745–757.
[29] C.A. Schneider, W.S. Rasband, K.W. Eliceiri, NIH image to ImageJ: 25 years of image analysis, Nat. Methods 9 (7) (2012) 671–675.
[30] W. Kabsch, Integration, scaling, space-group assignment and post-refinement, Acta Crystallogr. Sect. D 66 (2) (2010) 133–144.
[31] J. Agirre, M. Atanasova, H. Bagdonas, C.B. Ballard, A. Basle, J. Beilsten-Edmands, K. Yamashita, et al., The CCP4 suite: integrative software for macromolecular crystallography, Acta Crystallogr. Sect. D 79 (6) (2023) 449–461.
[32] P. Emsley, K. Cowtan, Coot: model-building tools for molecular graphics, Acta Crystallogr. Sect. D 60 (12) (2004) 2126–2132.
[33] D. Liebschner, P.V. Afonine, M.L. Baker, G. Bunkoczi, V.B. Chen, T.I. Croll, , et al.P. D. Adams, Macromolecular structure determination using X-rays, neutrons and electrons: recent developments in Phenix, Acta Crystallogr. Sect. D 75 (10) (2019) 861–877.
[34] E. Krissinel, K. Henrick, Inference of macromolecular assemblies from crystalline state, J. Mol. Biol. 372 (3) (2007) 774–797.
[35] J.L. Watson, D. Juergens, N.R. Bennett, B.L. Trippe, J. Yim, H.E. Eisenach, , et al. D. Baker, De novo design of protein structure and function with RFdiffusion, Nature 620 (7976) (2023) 1089–1100.
[36] B.L. Hie, V.R. Shanker, D. Xu, T.U.J. Bruun, P.A. Weidenbacher, S. Tang, P.S. Kim, et al., Efficient evolution of human antibodies from general protein language models, Nat. Biotechnol. 42 (2) (2024) 275–283.
[37] J. Frazer, P. Notin, M. Dias, A. Gomez, J.K. Min, K. Brock, , et al.D.S. Marks, Disease variant prediction with deep generative models of evolutionary data, Nature 599 (7883) (2021) 91–95.
[38] P. Tian, A. Lemaire, F. Sénéchal, O. Habrylo, V. Antonietti, P. Sonnet, D. Mercadante, et al., Design of a protein with improved thermal stability by an evolution-based generative model, Angew. Chem. Int. Ed. 61 (50) (2022) e202202711.
[39] R. Michael, J. Kæstel-Hansen, P. Mørch Groth, S. Bartels, J. Salomon, P. Tian, W. Boomsma, et al., A systematic analysis of regression models for protein engineering, PLoS Comput. Biol. 20 (5) (2024) e1012061.
[40] P. Tian, J.M. Louis, J.L. Baber, A. Aniana, R.B. Best, Co-evolutionary fitness landscapes for sequence design, Angew. Chem. Int. Ed. 57 (20) (2018) 5674–5678.
[41] D.E. Otzen, Conformational detours during folding of a collapsed state, Biochim. Biophys. Acta 1750 (2101) (2005) 146–153.
[42] K. Lindorff-Larsen, K. Teilum, Linking thermodynamics and measurements of protein stability, Protein Eng. Des. Sel. 34 (2021) gzab002.
[43] K.K. Andersen, H. Wang, D.E. Otzen, A kinetic analysis of the folding and unfolding of OmpA in urea and guanidinium chloride: single and parallel pathways, Biochemistry 51 (2012) 8371–8383.
[44] L. Baugh, L.A. Gallagher, R. Patrapuvich, M.C. Clifton, A.S. Gardberg, T. E. Edwards, , et al.W.C. Van Voorhis, Combining functional and structural genomics to sample the essential Burkholderia structome, PLoS One 8 (1) (2013) e53851.
[45] S. Romero-Romero, M. Costas, A. Rodríguez-Romero, D. Alejandro Fernández-Velasco, Reversibility and two state behaviour in the thermal unfolding of oligomeric TIM barrel proteins, Phys. Chem. Chem. Phys. 17 (32) (2015) 20699–20714.

[46] [dataset] G.e.a. Minasov, 1.65 Angstrom Crystal Structure of Triosephosphate Isomerase (TIM) from *Streptococcus pneumoniae*, 2023, https://doi.org/10.2210/pdb5IBX/pdb.
[47] E. Krissinel, K. Henrick, Inference of macromolecular assemblies from crystalline state, J. Mol. Biol. 372 (3) (2007) 774–797.
[48] Protein interfaces, surfaces and assemblies' service PISA at the European Bioinformatics Institute, 2025.
[49] B. Hernández-Ochoa, S. Gómez-Manzo, E. Alcaraz-Carmona, H. Serrano-Posada, S. Centeno-Leija, R. Arreguin-Espinosa, E. Sierra-Palacios, et al., Gene cloning, recombinant expression, characterization, and molecular modeling of the glycolytic enzyme triosephosphate isomerase from Fusarium oxysporum, Microorganisms 8 (1) (2020) 40.
[50] N.C. Pace, J.M. Scholtz, Measuring the conformational stability of a protein, in: T. E. Creighton (Ed.), Protein Structure: A Practical Approach, Oxford University Press, 1989, pp. 299–321.
[51] D.E. Otzen, O. Kristensen, M. Proctor, O. Oliveberg, Structural changes in the transition state of protein folding: an alternative interpretation of curved chevron plots, Biochemistry 1999 (38) (1809) 6499–6511.
[52] M.J. Parker, J. Spencer, A.R. Clarke, An integrated kinetic analysis of intermediates and transition states in protein folding reactions, J. Mol. Biol. 253 (880) (1995) 771–786.
[53] E. Jurrus, D. Engel, K. Star, K. Monson, J. Brandi, L.E. Felberg, N.A. Baker, et al., Improvements to the APBS biomolecular solvation software suite, Protein Sci. 27 (1) (2018) 112–128.